C L E A R A N D C L O U D - C A P P E D

MIXED LAYERS :
THEIR NUMERICAL SIMULATION, STRUCTURE AND GROWTH AND PARAMETERIZATION

B Y

J. W. D E A R D O R F F

NATIONAL CENTER FOR ATMOSPHERIC RESEARCH*, BOULDER, COLORADO 80303

U. S. A.

* The National Center for Atmospheric Research is sponsored by the National Science Foundation.

INTRODUCTION

Any comprehensive parameterization of the atmospheric boundary layer for use within a numerical weather forecast model must attempt to predict the height of the boundary layer and the occurrence of convective or stratiform clouds at its top. The deep boundary layers are of the most importance, as they modify the most tropospheric air. They grow and become deep mostly by a process called "entrainment" whereby turbulent air just below the top of the boundary layer tends to mix with, or entrap, the non-turbulent air just above.

In recent years, theoretical studies of boundary-layer entrainment over a heated surface in the absence of boundary-layer cloudiness (Lilly, 1967; Carson, 1973; Betts, 1973; Tennekes, 1973: Mahrt and Lenschow, 1976) have yielded satisfactory solutions for the entrainment rate. Often, however, boundary-layer clouds do develop which affect the entrainment rate and invalidate the clear air theoretical solution. Towering cumulus clouds remove air from the subcloud layer, or mixed layer, and thereby retard the growth rate of the latter. On the other hand, a stratocumulus-capped mixed layer having a capping inversion which prevents upward protruding turrets entrains at a rate many times greater than would a clear air mixed layer with the same capping inversion. Obviously, the forecast model must treat also these cloud effects within its boundary-layer parameterization if the latter is to possess any generality.

This particular series of lectures therefore mainly addresses the problem of the cloud-capped or cumulus-capped mixed layer. We make use of three-dimensional model simulations because observations of quantities relevant for the parameterizations, such as vertical fluxes of heat and moisture near the top of the boundary layer, are mostly lacking or nonexistent for cases when the boundary-layer clouds are present. Finally, we present some preliminary results of testing a comprehensive boundary-layer parameterization within NCAR's Global Circulation Model.

1. Numerical modeling of the unsaturated mixed layer

1.1 Brief description of the three-dimensional model

We start with a very brief description of the numerical model of the unsaturated boundary layer which has proved helpful in parameterizing its entrainment rate. This is the model of Deardorff (1972, 1974).

The later versions of this model have used a spatial grid network of $40 \times 40 \times 40$ grid points within a domain of area 5 km $\times$ 5 km and depth 2 km. (In the stratocumulus model the horizontal domain was shrunk to 2 km $\times$ 2 km). The non-hydrostatic, primitive, Boussinesq-approximated equations with all coriolis terms included are utilized in three dimensions on the "space-staggered" finite-difference grid shown in Fig. 1.1. The spatial derivatives have second-order accuracy on this grid, using Arakawa's (1966) energy conserving flux form of finite differencing. Time differencing was by the second-order Adams-Bashforth method (Lilly, 1965) using a time step of about 5 seconds.

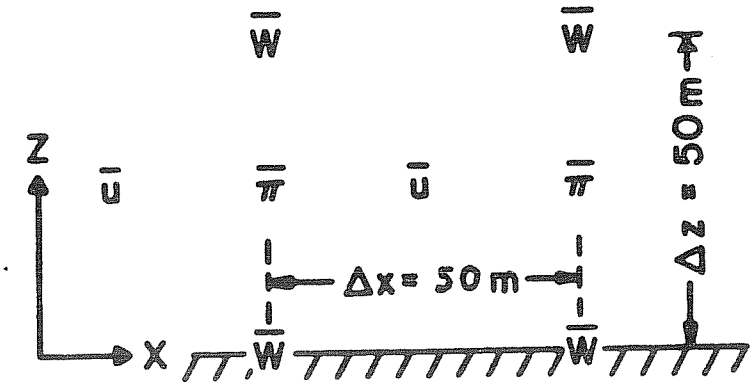

Fig. 1.1. The space staggered grid in the x-z plane. $\bar{\pi}$ represents pressure divided by mean density. $\bar{\theta}_l$ and $\bar{q}_w$ were positioned at the same points as $\bar{w}$.

The calculated value of a variable is considered to represent the mean value averaged over the surrounding grid volume, and is denoted by the overbar ($\bar{\ }$). Boundary conditions were that $w = 0$ at each grid point at the lower (horizontal) boundary, and also $\bar{w} = 0$ at the height $z = 2$ km, where $\partial\bar{u}/\partial z$, $\partial v/\partial z$ and $\partial w/\partial z$ were also set to zero. Lateral boundary conditions were cyclic, meaning that the longest horizontal wavelengths which could be represented were equal to the respective lengths of the domain. Lower boundary conditions amounted to deriving the turbulent fluxes at the surface (on the subgrid scale), and this was effected by use of the bulk aerodynamic method with a calculated time-dependent ground temperature, soil moisture, and a specified roughness length. The ground temperature was taken to be uniform horizontally. The surface fluxes were generally such as to transfer both sensible and latent heat upwards.

The entire model domain was allowed to advect uniformly in the downstream direction with a speed comparable to that of the overall mean wind, in order that spatial truncation errors in the downstream direction be no larger than those in the other two directions. Large-scale horizontal gradients of temperature, wind and humidity were assumed zero, while a large-scale horizontal pressure gradient was prescribed such as to give a geostrophic wind speed of about 4 m s^{-1}.

Turbulent fluxes on the subgrid scale were parameterized more simply than by the use of the full set of second-moment equations of Deardorff (1974). Instead, only for the subgrid-scale turbulence energy, $\bar{E}(x,t) = \frac{1}{2}(\overline{u'^2} + \overline{v'^2} + \overline{w'^2})$, was a time-dependent transport equation utilized:

$$\frac{\partial}{\partial t}\bar{E}^{1/2} = -\frac{\delta}{\partial x_i}\left(\bar{u}_i \bar{E}^{1/2}\right) + \frac{1}{2}\frac{K_m}{\bar{E}^{1/2}}\left[-\frac{g}{\bar{\theta}}\frac{K_h}{K_m}\frac{\partial\bar{\theta}_v}{\partial z} + \frac{1}{2}\left(\frac{\partial\bar{u}_i}{\partial x_j} + \frac{\partial\bar{u}_j}{\partial x_i}\right)^2\right] + K_m\nabla^2\bar{E}^{1/2} - \frac{1}{l}C_\varepsilon\bar{E} \qquad (1.1)$$

where K_m, K_h are subgrid-scale eddy coefficients for momentum and heat, θ_v is the virtual potential temperature, c_E is a constant in the dissipation term, and ℓ is a small-scale mixing length equal to or smaller than the representative grid length Δ:

$$\Delta = (\Delta x \cdot \Delta y \cdot \Delta z)^{1/3} \tag{1.2}$$

where Δx_i is the grid interval in the x_i direction. If Eq (1.1) is multiplied by $2\bar{E}^{\frac{1}{2}}$ it takes on the appearance of the turbulent energy equation.

The approximations utilized for the subgrid-scale turbulent fluxes are

$$\overline{u_i' u_j'} = \tfrac{2}{3}\delta_{ij}\bar{E} - K_m(\partial \bar{u}_i/\partial x_j + \partial \bar{u}_j/\partial x_i) \tag{1.3a}$$

$$\overline{u_i' \theta'} = -(K_h/K_m) K_m \partial \bar{\theta}/\partial x_i \tag{1.3b}$$

$$\overline{u_i' q'} = -(K_h/K_m) K_m \partial \bar{q}/\partial x_i \tag{1.3c}$$

where θ is potential temperature and q is specific humidity.

The subgrid-scale eddy coefficients appearing in the above equations are assumed given by

$$K_m = 0.10 \bar{E}^{1/2} \ell \tag{1.4}$$

$$K_h/K_m = 1 + 2\ell/\Delta \tag{1.5}$$

while the small-scale mixing length, ℓ, is assumed given by

$$\ell = 0.76 \bar{E}^{1/2} / \left(\frac{g}{\theta} \partial \bar{\theta}_v/\partial z\right)^{1/2} \quad \text{(when stable)} \tag{1.6a}$$

provided

$$\ell \leq \Delta \tag{1.6b}$$

For flow which is locally unstable thermally, ℓ is assumed given by

$$\ell = \Delta \quad \text{(when unstable)} \tag{1.6c}$$

Finally, c_E in Eq (1.1) is specified as

$$c_E = 0.188 + 0.512\, \ell/\Delta \tag{1.7}$$

such that $c_E = .70$ in locally unstable flow, and $c_E \to .188$ as the stable limit of no turbulence is approached. The latter value in conjunction with Eqs (1.1), (1.4) and (1.6a) corresponds to a critical value for the local Richardson number of 0.2. Thus, the subgrid-scale eddy coefficient, using this method, included the influence of local stability as well as that of advection and diffusion. Although the subgrid-scale fluxes are constrained by Eqs (1.3) not to transport a property counter to its gradient, this property is not forced upon the resolvable-scale flow field which can and has (Deardorff, 1972) yielded countergradient fluxes in the mean over selected regions of space.

This model with $(40)^3$ grid points requires 18 sec of "CPU" time on NCAR's CDC 7600 computer to calculate one (5-sec) time step; however, it runs 2½ times faster than my (1974) model which utilized the full set of 15 subgrid-scale transport equations (for $\overline{u_i'u_j'}$, $\overline{u_i'\theta'}$, $\overline{u_i'q'}$, $\overline{\theta'^2}$, $\overline{q'^2}$ and $\overline{\theta'q'}$). No deterioration of results using the simpler scheme was detected, apparently because the most important features (that K_m, K_h be stability dependent in a reasonable manner, and that K_h exceed K_m with unstable stability) are compatible with the essence of the more complicated scheme.

1.2 Derived structure and growth of the mixed layer

1.2.1 With surface heating alone. Elements of the mean structure derived for the clear daytime mixed layer by the model are shown in Fig. 1.2 for $\langle\bar{\theta}\rangle$, $\langle w\,\theta_v\rangle$ and $\langle q\rangle$ when the boundary layer stability was characterized by $-h/L = 200$, where h is the boundary layer height and L is the surface-based Monin-Obukhov length (the friction velocity, u_*, was about 20 cm s^{-1}). This stability value means that above a height of h/200, the turbulence energy was maintained more by the buoyancy force $((g/\theta)\langle w\theta_v\rangle)$ than by wind shear. (The angular brackets indicate the horizontal average of a quantity.) Above z = h the Richardson number greatly exeeds ¼ and the turbulence cannot penetrate far. The height h can be ascertained quite definitely in Fig. 1.2 from any one of the three profiles of heat flux, potential temperature, and specific humidity. The $\langle\bar{\theta}\rangle$ and $\langle\bar{q}\rangle$ profiles look just like any number of (smoothed) atmospheric profiles, especially those of Clarke et al. (1971, DAY 33) of which it is a simulation, and the heat-flux profile looks just like the mid-day profiles derived by Cattle and Weston (1975) over southern England during fair weather.

In a vertical x-z plane the numerically calculated turbulence structure of $\bar{w}$ and $\bar{\theta}$ is portrayed in Fig. 1.3 for the same time as in Fig. 1.2 (39 other vertical x-z planes could also have been portrayed.) The thermals which give rise to the major updrafts, and the correlation between the two, are clearly evident. The much smaller scale of the thermal eddies below x = .2h may also be noted, as well as the internal waves above z = h which do not support any diffusive turbulence. Regions of forced entrainment between updrafts, where $\bar{w} < 0$ and $\bar{\theta} > \langle\bar{\theta}\rangle$, especially as denoted by the arrows, are also evident. Such regions are responsible for the layer of negative heat flux in Fig. 1.2. Kelvin-Helmholtz instabilities associated with wind shear at z = h are not a necessary ingredient of the entrainment, although when present, the entrainment rate is expected to be increased.

The rate of entrainment, w_e, is found to be given by Lilly's (1968) kinematic relationship

$$w_e = \frac{dh}{dt} - \langle\bar{w}_h\rangle = -\langle\overline{w\theta_v}\rangle_h \,/\, \Delta\theta_v \tag{1.8}$$

where $\Delta\theta_v$ is defined as in Fig. 1.2, and $\langle\overline{w\,\theta_v}\rangle_h$ is a maximum negative value obtained by upward linear extrapolation from well below z = h up to z = h. Usually, $\Delta\theta_v$ cannot be ascertained accurately from observations unless it exceeds a degree or more. With this definition of $\langle\overline{w\theta_v}\rangle_h$, its negative value is usually found to be .2 to .3 of the surface flux of $\langle w\theta_v\rangle$.

1.2.2 With "dry-cloud"-top radiative cooling alone. In the absence of surface heating, the turbulence within a mixed layer can still be maintained by radiative cooling at the top of a stratocumulus deck which caps the mixed layer. The sinking of columns of cool air from z = h will drive convective turbulence in the mixed layer just as will the rising of columns of warm air upward from z = 0. Before treating the realistic stratocumulus case, however, the previous unsaturated case was pursued with a constant value of radiative cooling inserted at a height just below z = h, as from a "dry" cloud radiating outward to space. This applied cooling rate of 130 K day^{-1} over a layer of thickness Δz = 50 m corresponds to an outward kinematic heat flux of ΔR = .075 m s^{-1}K, and to a net cooling rate over a 1200 m mixed layer of 5.4 K day^{-1}. The ground temperature was adjusted downward so that the surface heat flux was approximately zero. The convective turbulence and mean profiles of $\bar{q}$ and $\bar{\theta}$ strongly resembled those of Figs. 1.2 and 1.3, with the exception being the absence of significant small-scale thermal plumes near the surface, and the presence of a very slight minimum in $\langle\bar{\theta}\rangle$ just below z = h where the radiative cooling was inserted.

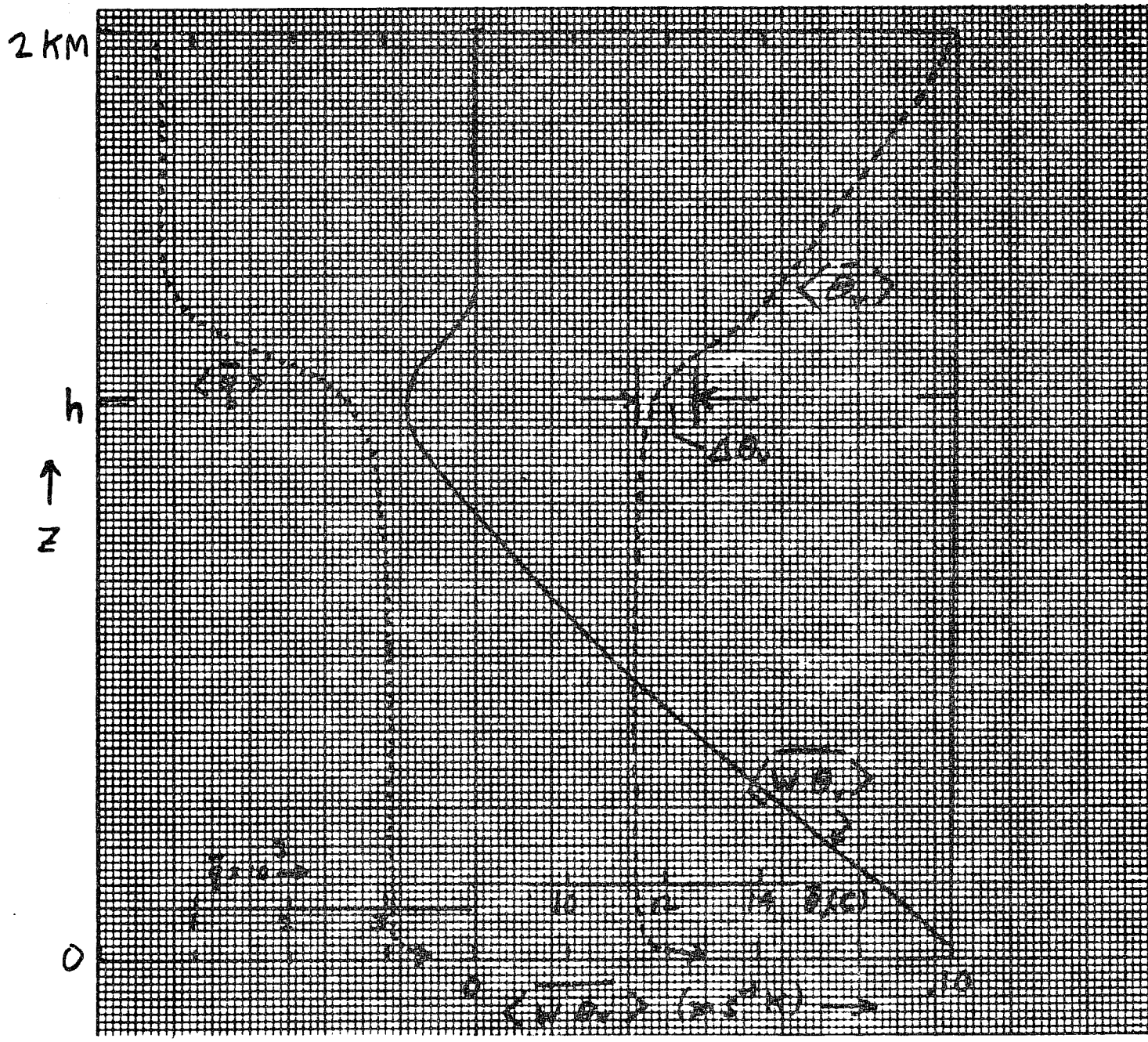

Fig. 1.2. Profiles of horizontally averaged $\bar{\theta}_v$, $\bar{q}$ and $\overline{w\theta}_v$ (the latter includes the subgrid scale contribution) of the mixed layer for the case of clear skies and turbulence driven mainly by surface heating.

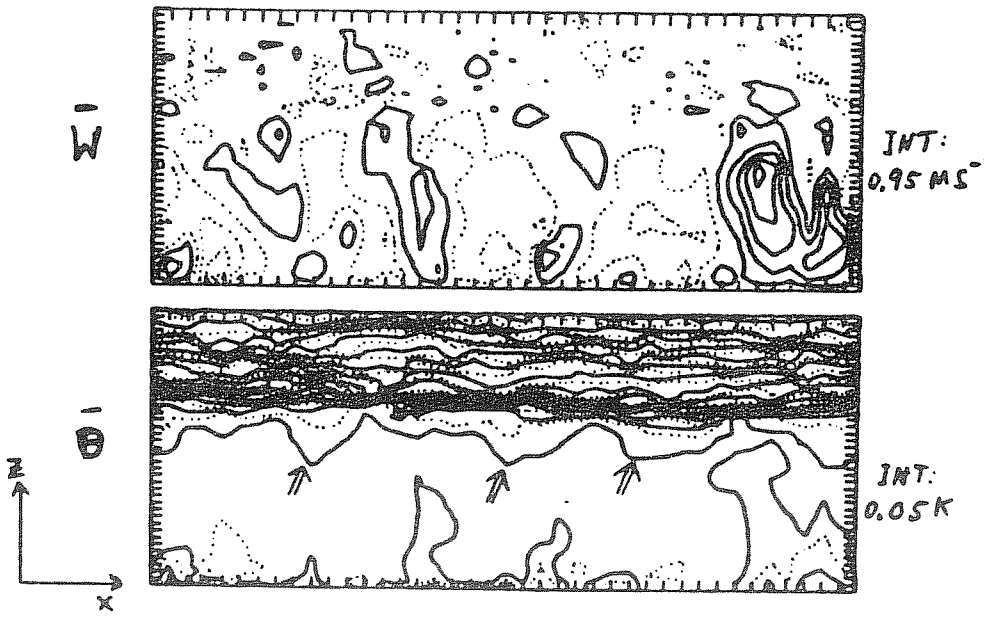

Fig. 1.3. The appearance of the numerically integrated values of $\bar{w}$ (upper portion) and $\bar{\theta}$ (lower) in a particular vertical plane of the 3-dimensional calculations for the same situation and time of Fig. 1.2. For $\bar{w}$, solid contours denote upward motion, dotted denote downward motion. For $\bar{\theta}$, every other contour line is dotted (interval between successive lines is 0.05K).

The turbulent heat-flux profile is now much different, however, as shown by the dashed curve in Fig. 1.4. Although it must again vary nearly linearly with height within the mixed layer, a jump occurs at the height of the simulated cloud top radiative cooling (between levels z_1 and h) such that the difference in $w'\theta_v'$ across the thickness Δz produces a warming which is counterbalanced by the divergence in outgoing radiative flux within the same layer. Hence, $\langle w\theta_v \rangle$ jumps to the left by the amount .075 m s^{-1}K in this case. Below this discontinuity, $\langle w\theta_v \rangle$ increases with height, showing that the radiative cooling gets distributed throughout the mixed layer and that the positive buoyancy force is present to maintain the convective turbulence. A negative heat-flux area just above z = h is again found, indicating that entrainment is again occurring and that the mixed layer is deepening. It is now evident, however, that the maximum negative heat flux of entrainment is not in general a function of the surface heat flux alone.

Eq.(1.8) in the presence of cloud top radiative cooling then becomes modified to

$$w_e = -\left[\langle \overline{w\theta_v} \rangle_1 - \Delta R\right] / \Delta\theta_v \qquad (1.9)$$

upon making use of $\langle \overline{w\theta_v} \rangle_1$ rather than $\langle \overline{w\theta_v} \rangle_h$.

This "dry-cloud" radiatively driven convection has been studied in the laboratory by McEwen and Paltridge (1976). They turned the system upside down and allowed short wave radiation to be absorbed into the bottom of a layer of colored water lying above a layer of clear, stably stratified quiescent water. The cloud layer (colored water) was found to be turbulent and to grow by entrainment (downwards) into the stable layer.

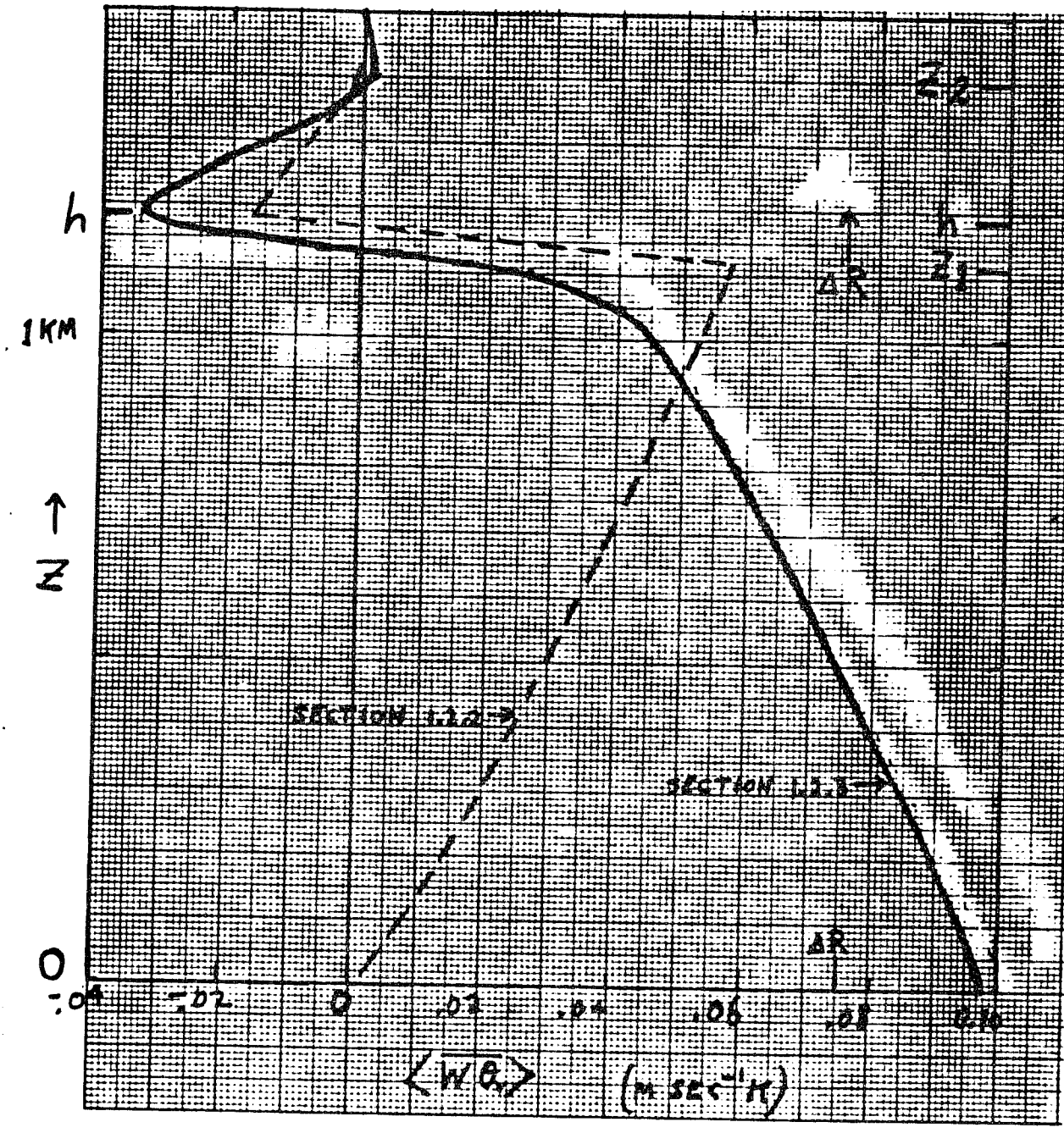

Fig. 1.4. Vertical profiles of $\langle \overline{w\theta_v} \rangle$ for the case of radiative cooling inserted at a level just above $z=z_1$. The dashed profile is with the absence of surface heating; the solid profile is with the presence of surface heating. This is the "dry"cloud case.

1.2.3 With both "dry-cloud"-top radiative cooling and surface heat flux. In this numerical integration, the conditions of the preceding section were altered only by increasing the ground temperature so as to produce a significant upward directed surface heat flux. The resulting profile of $\langle \overline{w\theta_v} \rangle$ after about an hour of simulated time is as shown in Fig. 1.4 by the solid curve. (It is more smeared out near z = h because it is an average over a longer time period (one-half hour during which h was rising more rapidly and the level of radiative cooling was shifted upwards.)

The negative heat flux of entrainment is now greater, since the turbulence in the mixed layer is more vigorous as driven both by surface heating and "dry-cloud"-top radiative cooling. Collectively, Figs. 1.2 and 1.4 suggest that the negative flux of entrainment, $\langle w\theta_v \rangle_h$, is more closely proportional to the mean value of $\langle w\theta_v \rangle$ within the mixed layer than to $\langle w\theta_v \rangle_0$; that is,

$$\langle w\theta_v \rangle_h \approx -k' \int_0^h \langle w\theta_v \rangle \, dz/h \tag{1.10}$$

where the value of k' seems to about 0.5. At the height designated z_1 in Fig. 1.4, however, $\langle w\theta_v \rangle$ can already be positive if ΔR is sufficiently large.

2. Numerical modelling of the stratocumulus-capped mixed layer

2.1 Use of liquid-water potential temperature, θ_ℓ, and total-water specific humidity, q_w.

Following Betts (1973), we make use of θ_ℓ defined as

$$\theta_\ell = \theta - \left(\frac{\theta}{T}\frac{L_v}{c_p}\right) q_\ell \tag{2.1}$$

where q_ℓ is the liquid-water specific humidity (mass of liquid water per mass of air), $\theta/T = (p_0/p)^{.286}$, L_v is the latent heat of vaporization, and c_p is the specific heat at constant pressure. To the extent that $(\theta/T)(L_v/c_p)$ is essentially constant following a parcel in comparison with q_ℓ, we see that the thermodynamic equation

$$\frac{d\theta}{dt} = \left(\frac{\theta}{T}\frac{L}{c_p}\right)\frac{dq_\ell}{dt} + \left(\frac{d\theta}{dt}\right)_{RAD} \tag{2.2}$$

can be rewritten as

$$\frac{d\theta_\ell}{dt} = \left(\frac{d\theta}{dt}\right)_{RAD} \tag{2.3}$$

where $(d\theta/dt)_{RAD}$ is the rate of change of θ due to radiative flux convergence. Hence, θ_ℓ is conserved during the liquid-water to vapor phase change, in the absence of radiative warming or cooling, just as is the equivalent potential temperature, θ_e, which may be similarly defined by

$$\theta_e = \theta_\ell + \left(\frac{\theta}{T}\frac{L}{c_p}\right) q \tag{2.4}$$

where q is the specific humidity, assumed equal to or less than the saturation value, q_s. Upon subtracting (2.1) from (2.4) we find that

$$\theta_e = \theta_\ell + \left(\frac{\theta}{T}\frac{L}{c_p}\right)(q + q_\ell) = \theta_\ell + \left(\frac{\theta}{T}\frac{L}{c_p}\right) q_w \tag{2.5}$$

where

$$q_w = q + q_\ell \tag{2.6}$$

The quantity q_w is the total-water specific humidity which is conserved in the absence of precipitation to the extent that cloud water is advected with the air. When $q_\ell > 0$, $q = q_s$ in (2.6); otherwise $q_w = q$ which is then also conserved. Hence, both θ_e and θ_ℓ are approximately conserved within a non-precipitating stratocumulus cloud. A convenience of using θ_ℓ, however, is that it becomes θ outside of the cloud. Hence, the change from a dry-convection model to a non-shallow non-precipitating liquid-water cloud model can be done simply by substituting θ_ℓ for θ and q_w for q, both in their conservation equations and in (1.3b) and (1.3c).

To obtain

$$\bar{\theta}_v = \bar{\theta}\,(1 + 0.61\,\bar{q} - \bar{q}_\ell) \tag{2.7}$$

for use in the model's vertical velocity equation, however, and for other reasons, one must know if the air is saturated or unsaturated. A method of obtaining $q_s(\theta_\ell, q_w, p)$ was presented by Deardorff (1976), so that q_ℓ can then be deduced with the aid of Eq (2.6), and θ and T from Eq (2.1). The dependence of the subgrid-scale vertical flux of θ_v, $\overline{w'\theta_v'}$, upon $\overline{w'\theta_\ell'}$ and $\overline{w'q_w'}$ from the modified versions of (1.3b) and (1.3c) also depends upon whether or not the air is saturated. These relationships are also given in Deardorff (1976). Since θ_v is not a conservative variable during condensation or evaporation, it is important that $\overline{w'\theta_v'}$ not be approximated by $-K_h\partial\overline{\theta_v}/\partial z$.

In the numerical results on stratocumulus to be presented, it was assumed that all the air within a grid volume is saturated if $\overline{q_w} > \overline{q_s}$, and all the air unsaturated if $\overline{q_w} < \overline{q_s}$. However, it is possible to relax this assumption if an estimate of $\sigma' = (\overline{q_w'^2} + \overline{q_s'^2} - 2\,\overline{q_w'q_s'})^{1/2}$ is available, in which case one finds some saturated air within a grid volume for $(\overline{q_w} - 1.6\,\sigma') < \overline{q_w} < \overline{q_s}$, and solid saturation only if $\overline{q_w}$ exceeds $\overline{q_s}$ by $1.6\,\sigma'$.

2.2 Results with stratocumulus throughout the mixed layer.

One case was integrated with the air so moist that the lifting condensation level occurred, on the average, at the small height $z_c = 0.1$ h. The mean surface fluxes of heat and moisture were $\langle w\theta_v\rangle_0 = .03$ m s^{-1}K, and $\langle wq\rangle_0 = 1.4 \times 10^{-5}$m s^{-1} Radiative cooling was imposed at the rate -1.5×10^{-3}K s^{-1} within the uppermost saturated grid volume (of thickness $\Delta z = 50$ m) of each vertical column.

Mean profiles and the vertical fluxes $\langle\overline{w\theta_v}\rangle$ and $\langle\overline{w\theta_e}\rangle$ existing at a particular time (hour 15.80) are shown in Fig. 2.1. Small wiggles in $\langle\overline{\theta_\ell}\rangle$, $\langle\overline{\theta_e}\rangle$ and $\langle\overline{q_w}\rangle$ profiles in the mixed layer, and larger wiggles in the vertical fluxes, are sampling errors associated with the averaging area (2 km × 2 km) being insufficiently large. Nevertheless, important features clearly identifiable include

(a) nearly uniform values of conservative quantities $\langle\overline{\theta_e}\rangle$, $\langle\overline{\theta_\ell}\rangle$ and $\langle\overline{q_w}\rangle$ in the lower 85% of the mixed layer above the surface layer, with $\langle\overline{\theta_\ell}\rangle$ and $\langle\overline{q_w}\rangle$ exhibiting poorly mixed "shoulders" in the upper 15%;

(b) a moist adiabatic lapse rate for $\langle\overline{\theta_v}\rangle$ within the stratocumulus layer;

(c) a linearly increasing liquid-water content from cloud base to a height of about 0.85 h;

(d) negative jumps in $\langle\overline{w\theta_v}\rangle$ and $\langle\overline{w\theta_e}\rangle$ at $z = h$ associated with radiative flux divergence;

(e) occurrence of the most negative buoyancy flux of entrainment at a level within the stratocumulus which is mostly saturated ($\sigma_c > \frac{1}{2}$), where σ_c is the cloud fraction at any given height.

If the cloud top had no undulations, so that the local radiative flux divergence all occurred at the same height (as in the "dry" cloud simulations), the jump in $\langle w\theta_e\rangle$ just below $z = h$ would have the value -7.5 cm s^{-1}K. The much smaller jump of about -2.2 cm s^{-1}K indicates that most of the radiative cooling is occurring in cloud domes penetrating into the inversion layer just above the mean value of h. Hence, most of the radiative cooling is used up in cooling the inversion layer, thus promoting entrainment indirectly. Lilly (1968) assumed that none of the radiative cooling occurs in the mean mixed layer in his stratocumulus entrainment theory, while in this numerical simulation about 30% occurred in the (upper) mean mixed layer.

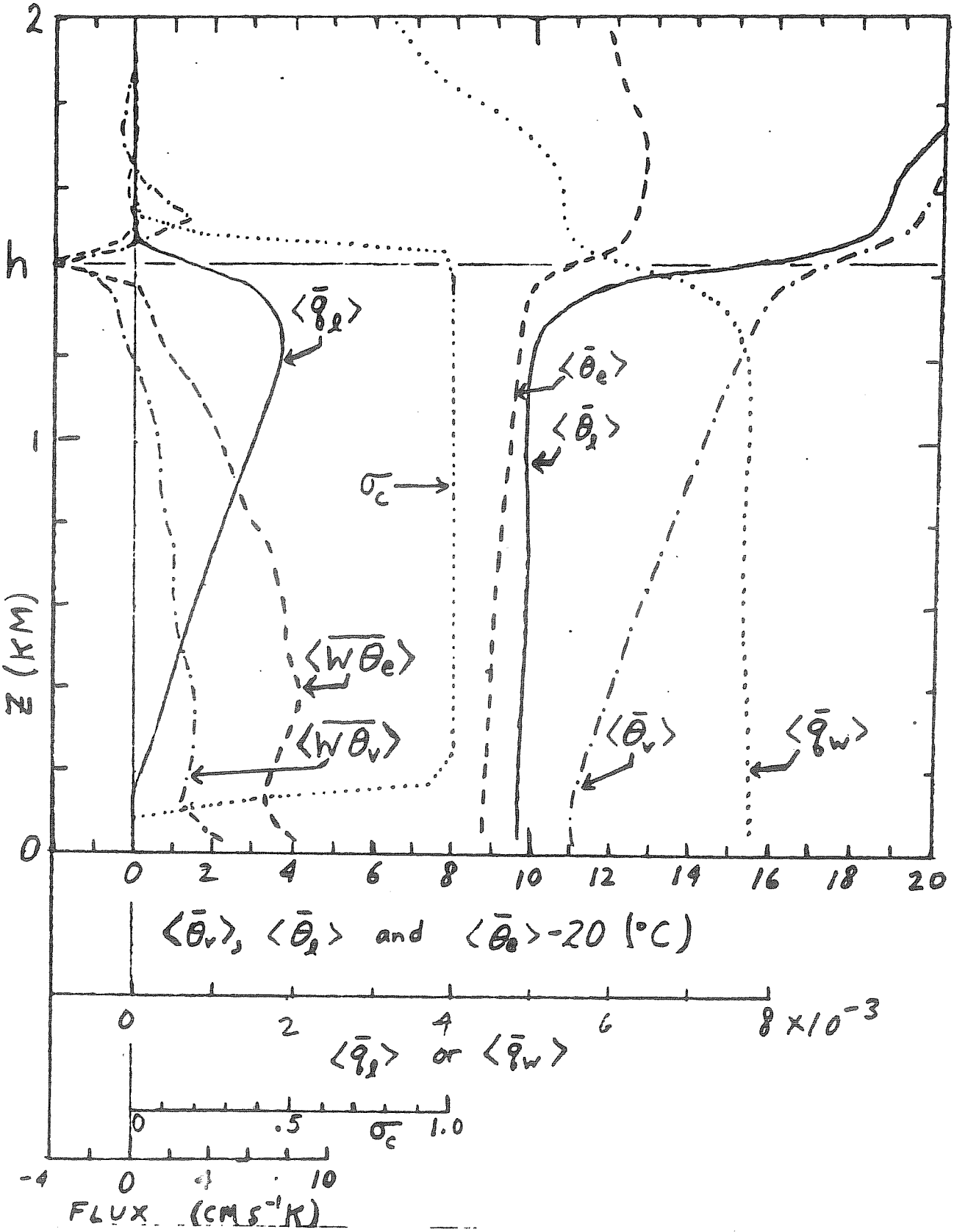

Fig. 2.1. Profiles of the horizontally averaged quantities: $\langle\bar{\theta}_v\rangle$, $\langle\bar{\theta}_\ell\rangle$, and $\langle\bar{\theta}_e\rangle$ in degrees C, upper abscissa; $\langle\bar{q}_\ell\rangle$ and $\langle\bar{q}_w\rangle$, second scale at bottom; fraction of area saturated at a given height, σ_c, third scale; and the fluxes $\langle\overline{w\theta_v}\rangle$ and $\langle\overline{w\theta_e}\rangle$, lowermost scale, existing at a particular time. Cloud base is at about 120m and cloud top at 1400m.

The magnitude of $\langle \overline{w\theta_v} \rangle_h$ appearing within a particular realization suffers from considerable sampling error because the areal domain is only 2 km × km. Averages of the vertical fluxes over 47 realizations spanning the simulated time period from hour 15.43 to 16.80 are shown in Fig. 2.2. Although sampling errors are now minimized, detailed structures in the vicinity of z = h are washed out because h grew from 1375 m to 1525 m. Hence the value of $\langle w\theta_v \rangle_h$ cannot be estimated from Fig. 2.2. The large value of moisture flux in the upper mixed layer is associated with entrainment of the drier air aloft down into the deepening stratocumulus-filled mixed layer.

The expected values of $\langle w\theta_e \rangle_1$ and $\langle wq_w \rangle_h$ as obtained by Lilly's (1968) method of layer integration across z = h are

$$\langle w\theta_e \rangle_1 = \Delta R - w_e \Delta\theta_e + \langle w\theta_e \rangle_2 \qquad (2.8a)$$

$$\langle wq_w \rangle_h \approx \langle wq_w \rangle_1 = - w_e \Delta q_w + \langle wq_w \rangle_2 \qquad (2.8b)$$

where $\Delta\theta_e$ and Δq_w are the "jumps" in $\langle\theta_e\rangle$ and $\langle q_w\rangle$ across z = h, from z_1 to z_2 (see Fig. 1.4). If the jump conditions are derived between z = h and z = z_2, and if the fraction of the radiative cooling which occurs in this inversion region is r ($0 \leq r \leq 1$), then (2.8a) becomes

$$\langle w\theta_e \rangle_h = r\Delta R - w_e \Delta\theta_e \qquad (2.8c)$$

The jump in $\langle\theta_e\rangle$ from Fig. 2.1 is about 2.3 K, and the jump in $\langle q_w\rangle$ across the same height interval is about -1.7×10^{-3}. From Fig. 2.2 the upward extrapolated value of $\langle w\theta_e \rangle$ linearly to z = z_1 or h is about 1.5 cm s^{-1} K, while $\langle wq_w \rangle_1 \approx 4.4 \times 10^{-3}$. With ΔR = 7.5 cm s^{-1} K, the values for w_e then obtained from (2.8a) and (2.8b) are 3.9 cm s^{-1}, and 2.6 cm s^{-1}, respectively; while the observed entrainment rate (dh/dt) during the 1.37 hour period was 3.1 cm s^{-1}. Although the agreement is satisfactory in the mean, the variation in $(\partial/\partial z)\langle w\theta_e \rangle$ near z = 1 km is unexplained and adds uncertainty to the estimate from (2.1a).

The positive blip in $\langle w\theta_v \rangle$ just above z = h occurred systematically but is unexplained. It occurred mainly on the resolvable scale, as opposed to the subgrid scale, and may have been caused by vertical truncation errors in the equations for θ_ℓ and q_w.

2.3 Results with stratocumulus in the upper mixed layer.

In this case radiative cooling at cloud top was applied as in section 2.2. However, the mean moisture content in the mixed layer was decreased, so that the cloud-base height turned out to be 650 m, when h was 1150 m, on the average. The root-mean-square cloud top excursion was 25 m.

The vertical profile of $\langle \overline{wq_w} \rangle$ appeared much the same as in Fig. 2.2, but the $\langle w\theta_v \rangle$ profile exhibited an additional discontinuity associated with the elevated cloud base. This profile is shown in Fig. 2.3, where the cloud base jump in $\langle \overline{w\theta_v} \rangle$ is as described by Schubert (1976). Fig. 2.3 averages over 14 realizations for a period of only 0.32 hours, so that the double-jump structure in $\langle w\theta_v \rangle$ in the vicinity of z = h remains clearly in evidence. Here it occurs at the height where the cloud fraction is only about 0.5.

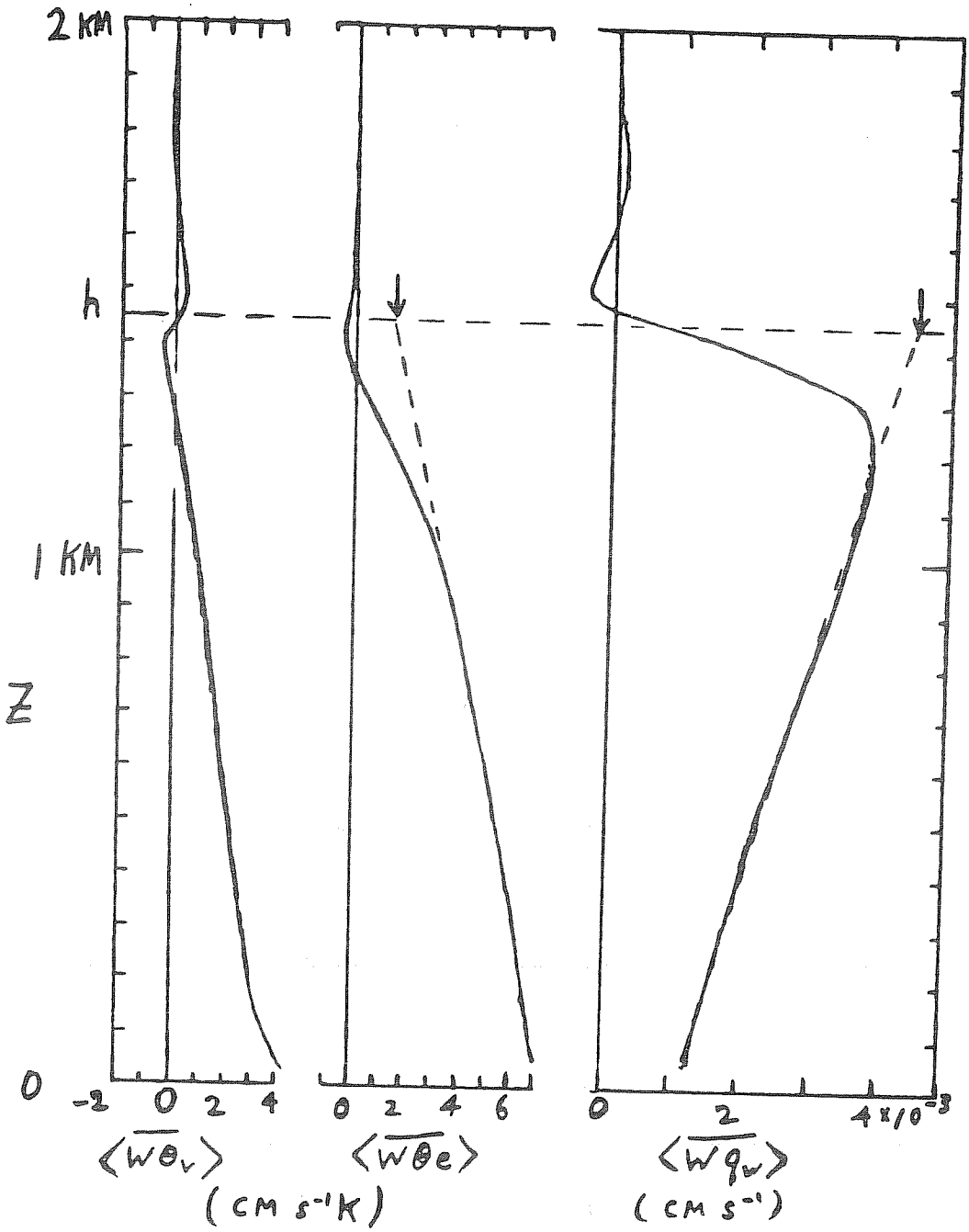

Fig. 2.2. Vertical profiles of $\langle \overline{w\theta}_v \rangle$, $\langle \overline{w\theta}_e \rangle$ and $\langle \overline{wq}_w \rangle$ for the same stratocumulus case as in Fig. 2.1 except that time averaging over a 1.37 hr period is employed as well as horizontal averaging. As before, the fluxes include the subgrid-scale contributions as well as the resolvable scale contributions. Arrows indicate upward extrapolated values applying just below z=h.

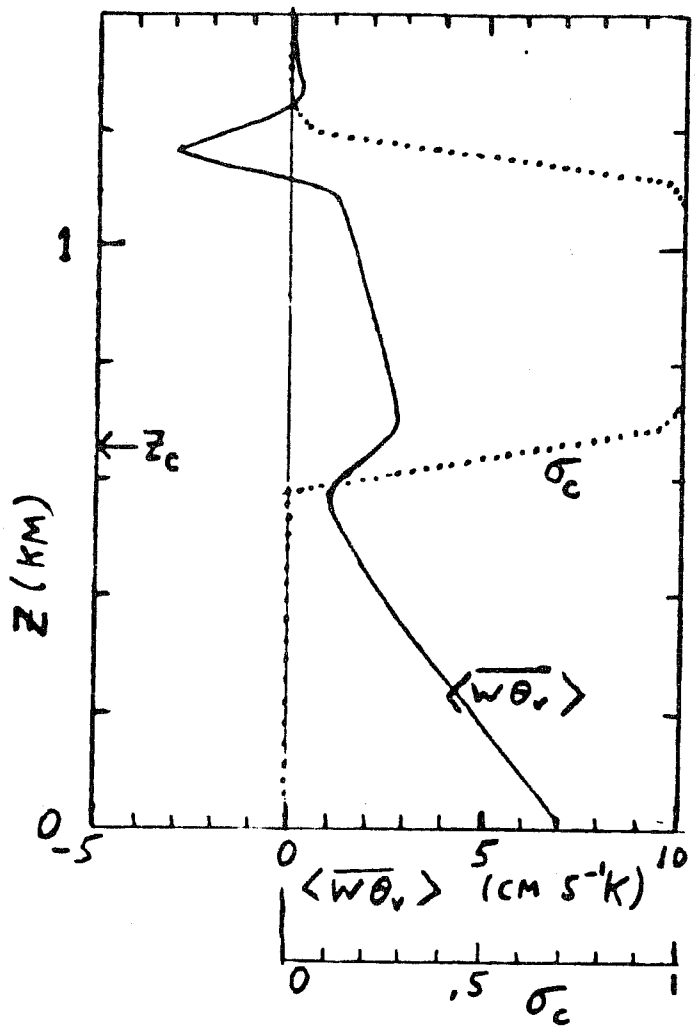

Fig. 2.3. Vertical profiles of $\langle \overline{w\theta_v} \rangle$ and local cloud fraction, σ_c, for the case of stratocumulus in the upper half of the mixed layer. The averaging is over a time period of 0.32 hrs.

As in Fig. 2.1, the negative value of $\langle \overline{w\theta_v} \rangle_h$ in this case is surprisingly large, and equals 1.1 of the $\langle \overline{w\theta_v} \rangle_{mean}$. This result suggests that a better closure assumption for $\langle w\theta_v \rangle_h$ than that discussed in section 1.2.3 might be to relate the negative area extending up to z_2 (on a plot of $\langle w\theta_v \rangle$ versus z) to the positive area below. If this procedure is applied to Figs. 1.2, 1.4, 2.1 and 2.3, one finds a ratio of negative area to positive area of 0.07 ± .022, which appears sufficiently significant and constant to be useful. However, application of this closure would require knowledge of the vertical extent of the transition layer above z = h and of the detailed shape of the $\langle w\theta_v \rangle$ profile in this region. Furthermore, the laboratory experiments of Willis and Deardorff (1974) suggest that the negative area becomes somewhat smaller, relative to the positive area, as the stability at z = h and above is increased.

Fig. 2.4 is a picture of the $\overline{\theta_\ell}$ and $\bar{w}$ eddies in a vertical x-z plane in this case. Although it is difficult to tell where cloud base is from these two variables, there frequently appeared to be a tendency for the $\bar{w}$ eddies in the cloud and sub-cloud layer to be somewhat distinct as in Fig. 2.4. This tendency results from the minimum in $\langle w\theta_v \rangle$ near cloud base (see Fig. 2.3) where there was also a weak minimum in vertical velocity variance.

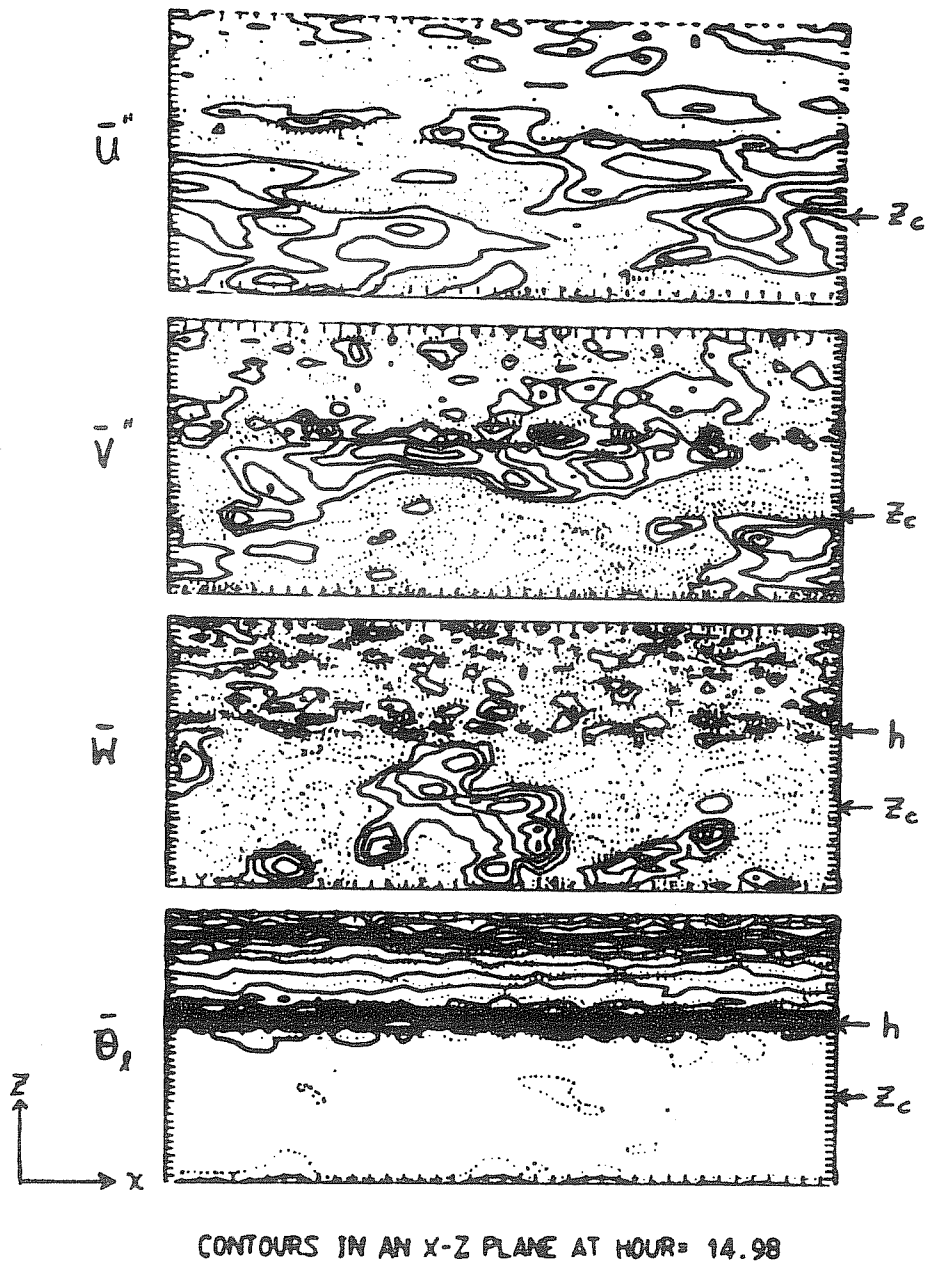

Fig. 2.4. Contours of $\bar{u}-\langle\bar{u}\rangle$, $\bar{v}-\langle\bar{v}\rangle$, $\bar{w}$ and $\bar{\theta}_\ell$ in a vertical plane for the case of stratocumulus occupying the upper half of the mixed layer. Contour intervals are 35 cm s^{-1}, 28 cm s^{-1}, 37 cm s^{-1} and 0.05K, respectively. Tick marks at edges depict grid intervals. Except for $\bar{\theta}_\ell$, solid contours represent positive values, dotted contours represent negative values.

The turbulence kinetic-energy balance for this case, obtained from three realizations, is shown in Fig. 2.5. Except below 50 m the wind-shear source term was negligible and is therefore not shown. Terms which are shown are buoyancy, dissipation (ε), turbulent diffusion on the resolvable scale ($-\frac{\partial}{\partial z}\langle \bar{w}''\bar{E}''\rangle$), and the pressure "diffusion" term on the resolvable scale, ($-\frac{\partial}{\partial z}\langle \bar{w}\bar{p}''/\rho_o\rangle$), where the ( )'' notation is defined by $\underline{u}'' = \underline{u} - \langle \underline{u}\rangle$ and has any large-scale mean removed. The remaining term, $-\frac{\partial}{\partial z}\langle \overline{w'(E'+p'/\rho_o)}\rangle$, is the sub-grid-scale turbulent diffusion term which may be obtained as a residual; it is not plotted. The buoyancy curve is proportional to $\langle \underline{w\theta_v}\rangle$ and has therefore already been discussed; the dissipation curve shows surprisingly large values just below cloud top which were not supported by any mean-shear generated turbulence, but is otherwise not unusual. The resolvable scale turbulent-diffusion term seems to sense the difference between the subcloud layer and stratocumulus layer; in the lower layer it behaves in the usual manner of being a sink in the lower portion and a source in the upper portion; however it is mostly a source in the cloud layer. The resolvable "pressure"-diffusion term tends to cancel a somewhat larger part of the resolvable turbulent-diffusion term than expected. In the bulk of the mixed layer the subgrid diffusion term is a rather small residual, but above z = .95 h it becomes very large in places. Since the assumption behind this term is not trusted here any more than it is in second-moment models, the energy-balance terms above this point cannot be trusted. However, it is not unreasonable to expect that this term should be relatively large close to the edges of the boundary layer where turbulence elements are forced to have small vertical scales, especially at the base of a stiff inversion.

2.4 Results for a breaking stratocumulus cloud deck

For this case the thermal stability characterized by $\Delta\theta_e$ at the top of the stratocumulus was reduced to only a few degrees, and then subsequently reduced further in small steps, by decreasing the temperature of the entire layer above $z = z_1$ and increasing the specific humidity. The purpose was to simulate the method by which an actual stratocumulus layer often breaks up, although in most actual cases $\Delta\theta_e$ decreases more because of the mixed layer warming up than because of the stable layer cooling.

Attention is focused upon $\Delta\theta_e$ because in a layer of saturated air a fluctuation in density or virtual temperature is proportional to a fluctuation in θ_e (except for the influence of fluctuations in liquid-water content). That is, a parcel of air just above cloud top of $\theta_e = \theta_{e1}$, when mixed downward until it is just saturated and incorporated into the stratocumulus, conserves its θ_e and finds itself surrounded by air of $\theta_e = \theta_{e1} - \Delta\theta_e$. Thus, if $\Delta\theta_e$ is negative, this parcel would be expected to be buoyant (more dense) and continue to sink downward into the cloud. The cloud would then become riddled with entraining air until holes appeared. Because of the influence of cloud water upon buoyancy, a somewhat negative value of $\Delta\theta_e$ is required before this instability commences. One cannot rely upon parcel instability arguments, however, because the domain under consideration is already turbulent (unstable) due to other causes.

The rate at which $\Delta\theta_e$ was decreased during the numerical simulation is shown in Fig. 2.6. Also shown are the vertical-mean cloud cover, $\overline{\sigma_c}$, and the entrainment rate, w_e. Only after $\Delta\theta_e$ was about -1 K did w_e increase significantly, but not catastrophically as most theories would indicate. At the same time, the cloud layer developed more and more regions of unsaturated air, as indicated by the decreasing slope of the $\overline{\sigma_c}$ curve. The distribution of cloud

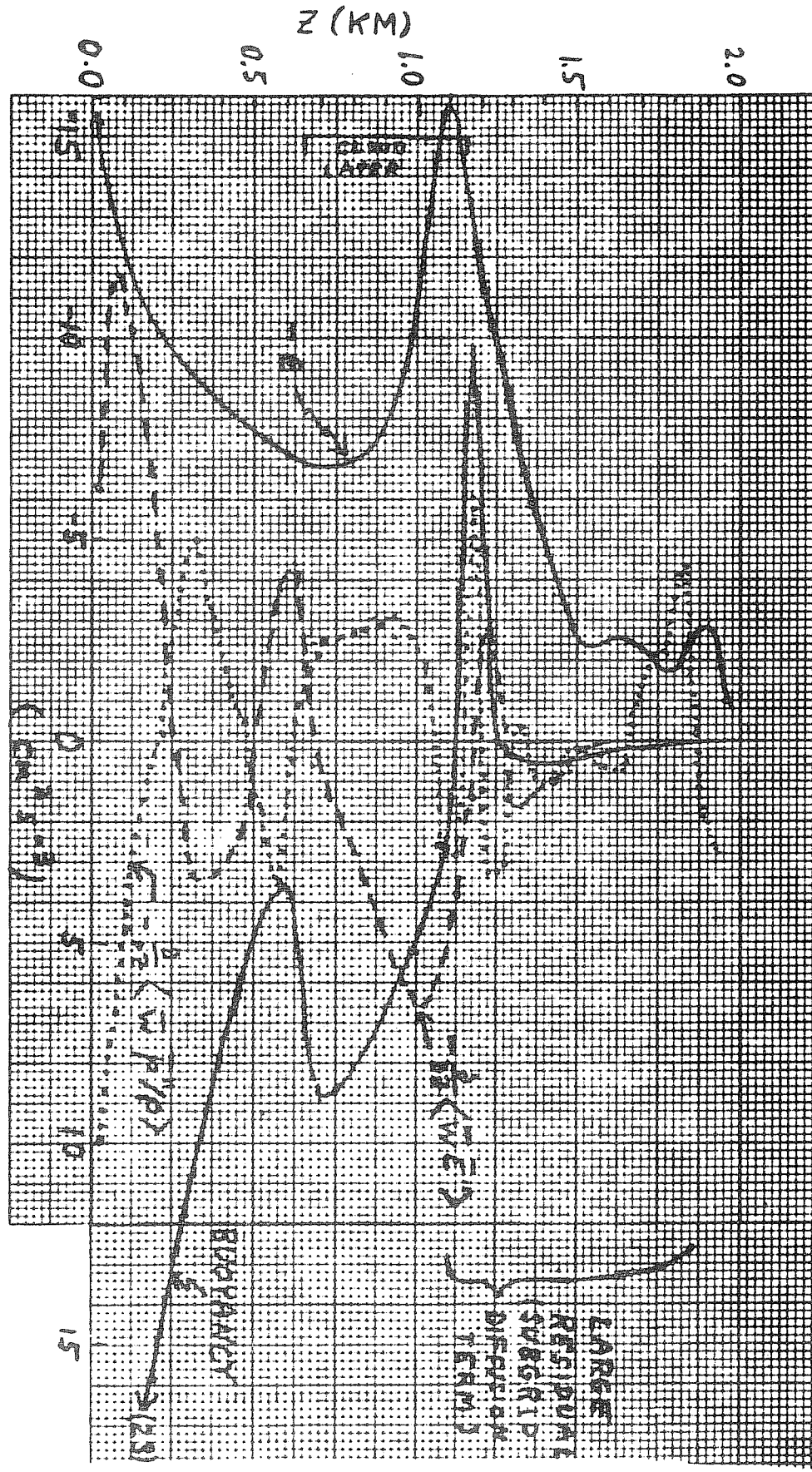

Fig. 2.5. Terms in the turbulence kinetic energy budget as a function of height for the case when stratocumulus occupied the upper half of the mixed layer. Shear-stress production was negligible, and the residual (not plotted) represent subgrid-scale turbulent diffusion.

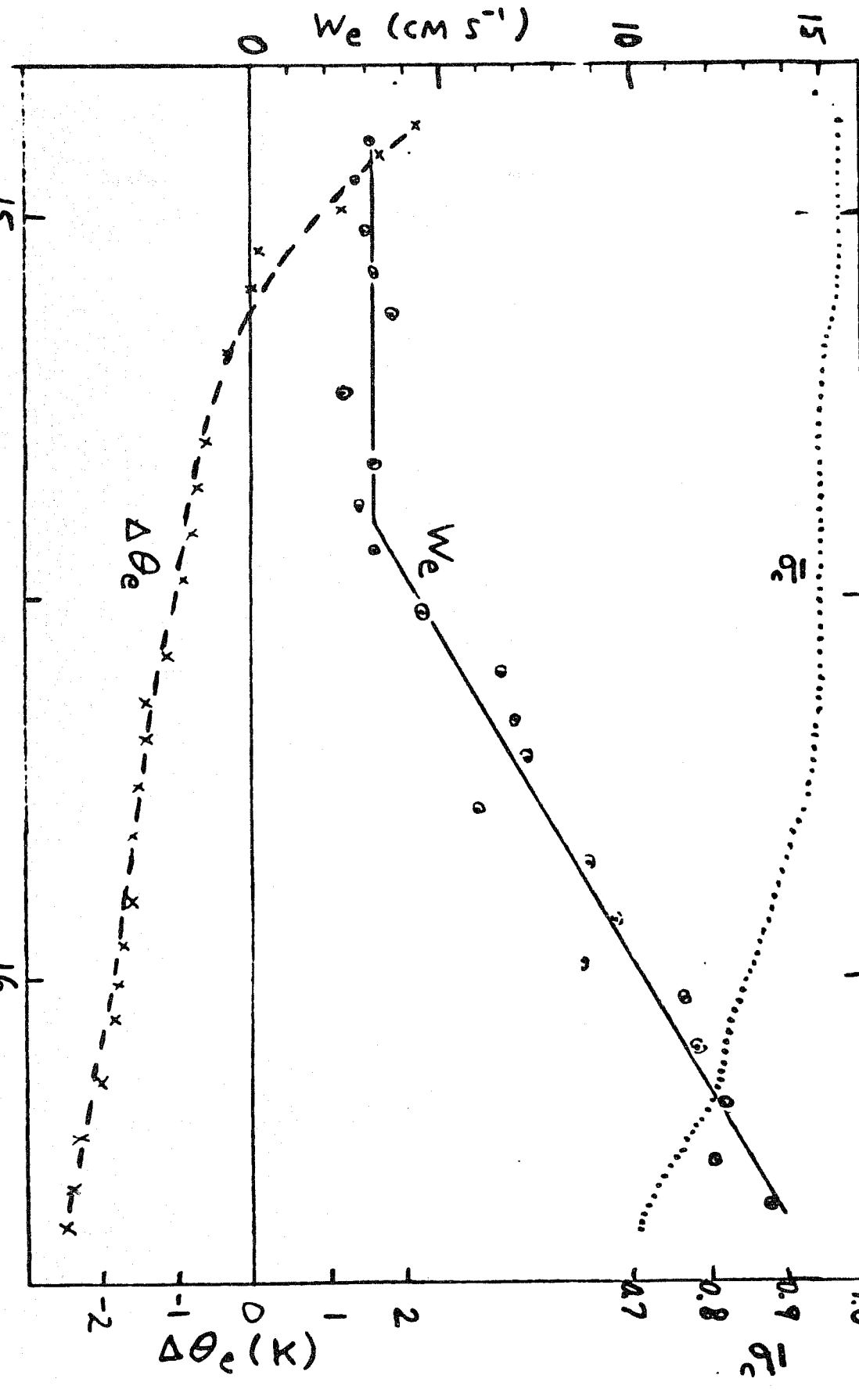

Fig. 2.6. Time dependence of $\Delta\theta_e$ (dashed curve and x's), entrainment rate (w_e, solid curve and circles), and vertically averaged cloud fraction (dotted curve) for the case of the breaking stratocumulus cloud.

fraction as a function of height at four times during the stratocumulus breakup is shown in Fig. 2.7. At the latter time the stratocumulus deck is no longer solid at any height, but shows the most drying out near cloud base, probably because the in-cloud liquid-water content increases nearly linearly with height.

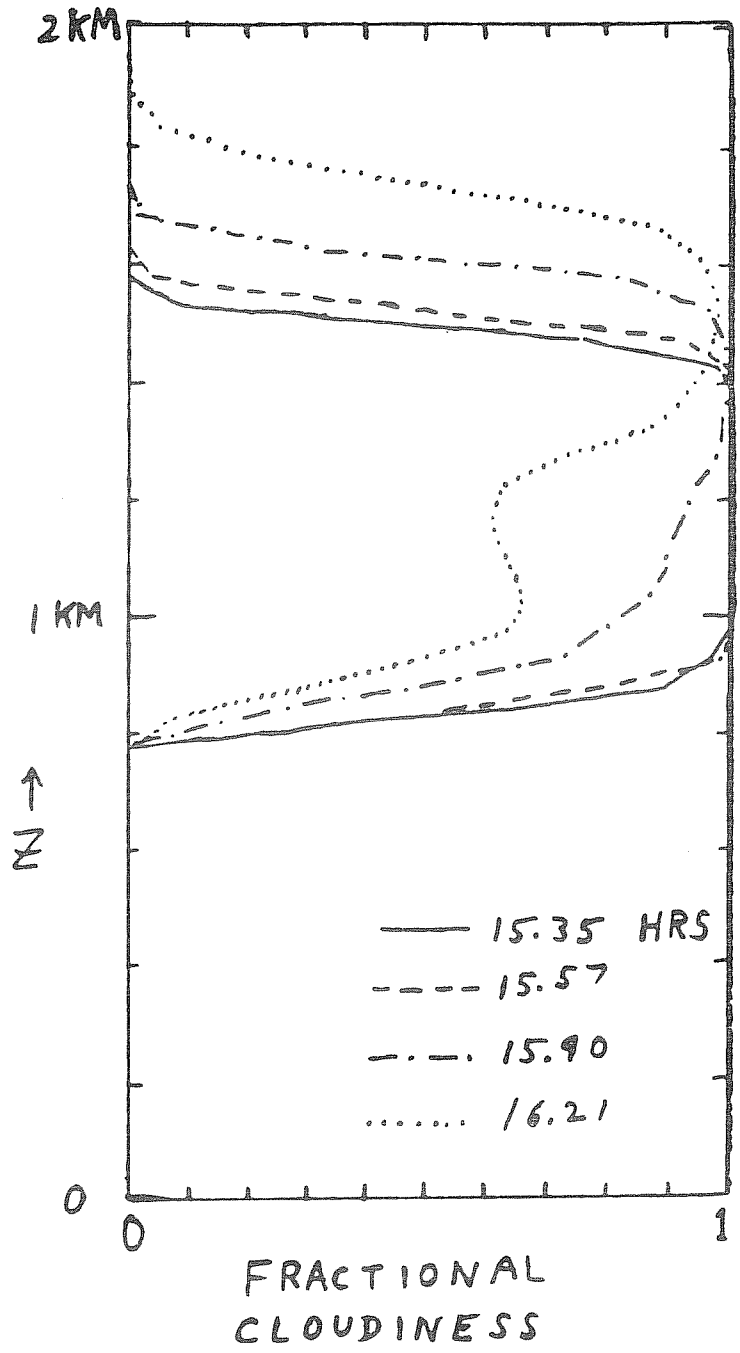

Fig. 2.7. Fraction of air saturated as a function of height at four successive times, from the numerical integration of the case of the breaking stratocumulus deck.

Unfortunately the integration could not be carried much beyond the stage depicted for hour 16.21 because the top of the boundary layer had reached too close to the top of the model at 2 km. Hence the evolution towards a scattered cumulus layer (with bases near 800 m and tops near 2 km) was not studied.

Mean profiles of $\langle\overline{\theta_e}\rangle$, $\langle\overline{q_w}\rangle$ and $\langle\overline{\theta_v}\rangle$ at the same four times are shown in Fig. 2.8. In the cloud layer, $\langle\theta_v\rangle$ evolves somewhat away from the moist adiabati lapse rate towards the dry adiabatic as the cloud layer begins to dry out. At th same time, $\langle q_w\rangle$ does not stay as well mixed in the cloud layer, while $\langle\theta e\rangle$ does.

The moisture flux profiles responsible for the drying of the cloud layer are shown in Fig. 2.9 at the same four times. Here we see most drastically that the well-mixed assumption for $\langle q_w\rangle$, which implies that $\langle wq_w\rangle$ be linear within the mixed layer, is grossly violated. As soon as significant gaps in cloud cover appear within the cloud deck, there is a large enhancement of $\langle\overline{wq_w}\rangle$ in the upper part of this layer which promotes a drying of the lower and middle cloud layer (and a moistening just above cloud top as the cloud tops rise). The main conclusions to be drawn are that the well-mixed assumption for moisture should not be invoked unless the entire cloud deck is solidly saturated, and that solid saturation should not be expected to be maintained if $\Delta\theta_e$ reaches a value as negative as about -1 K. (With thinner cloud layers a less negative value would be required.)

For parameterization purposes, therefore, studies of a fully saturated stratocumulus-mixed layer may provide useful information on w_e for the limiting case, but provide no justification for extrapolating any formulations so obtained towards the partly-cloudy regime. In the latter regime, of course, it is recognized that the cloud layer does not communicate freely with the subcloud layer, and that the two layers together are in no sense well mixed. Hence, the subcloud and the cloud layers are usually parameterized distinctly within numerical prediction models.

3. Entrainment rate theories

3.1 The unsaturated mixed layer

3.1.1 Forced entrainment. When a substantial increase in thermal stability occurs at the top of the mixed layer ($\Delta\theta_v$ greater than a few tenths of a degree), Eq (1.8) for w_e may be utilized to predict the entrainment rate after $-\langle w\theta_v\rangle_h$ is approximated by $k\langle w\theta_v\rangle_0$. Then we find

$$(w_e)_{forced} = k\langle w\theta_v\rangle_0 / \Delta\theta_v \qquad (k \sim .2 \text{ to } .3) \quad (3.1)$$

to be a useful method of obtaining w_e in the case of no boundary-layer cloudiness. The entrainment in this (usual) case is here called "forced", since work must be done at the interface to force some of the overlying warm air downwards into the cooler mixed layer.

3.1.2 Encroachment. If $\Delta\theta_v$ is very small, an assumption in the derivation of (1.8) becomes invalid; i.e., that

$$\left| \frac{\partial}{\partial t} \int_{z_1}^{z_2} \theta_v \, dz \right| \ll w_e \Delta\theta_v$$

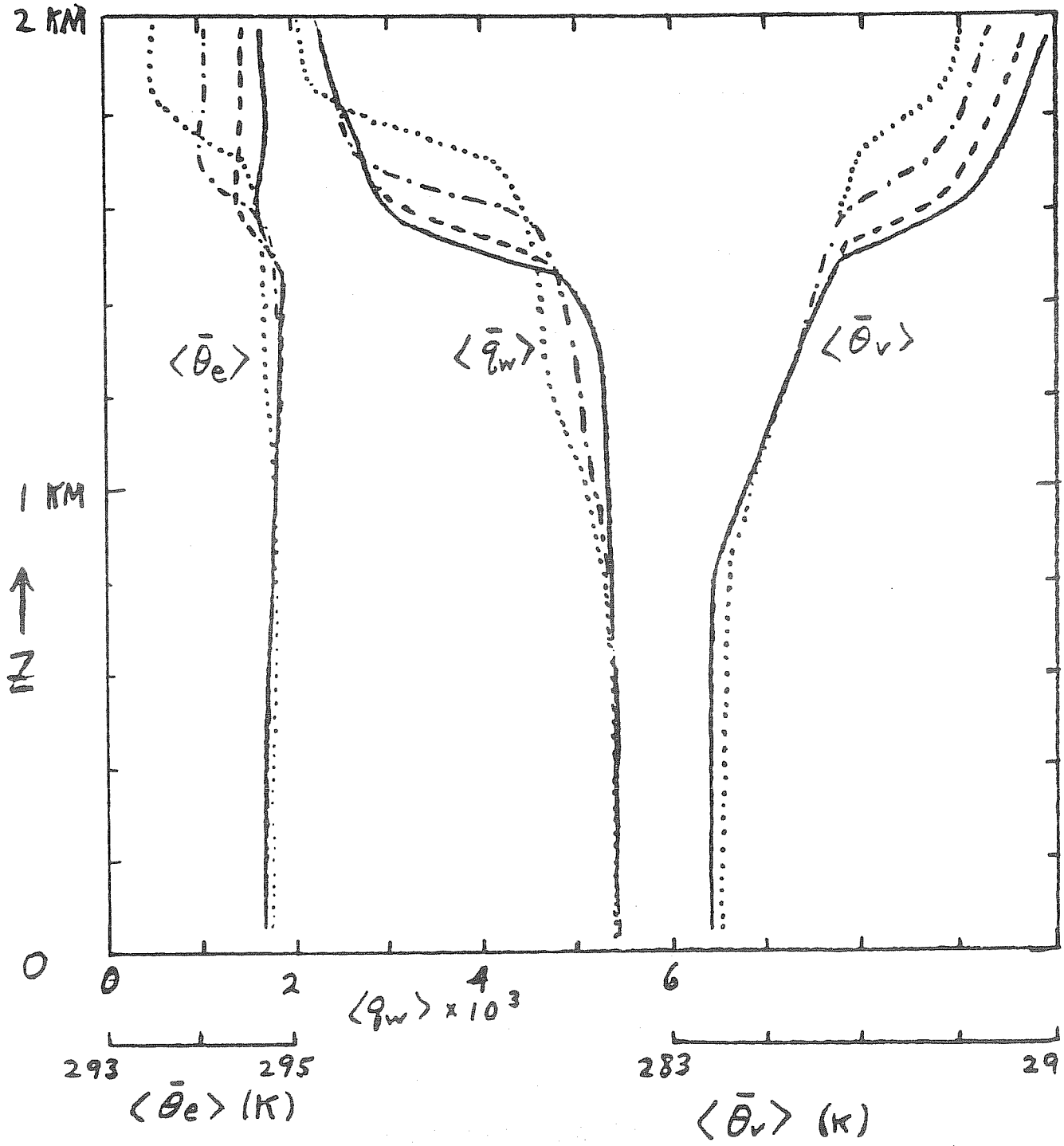

Fig. 2.8. Vertical profiles of the horizontally averaged values calculated for $\bar{\theta}_e$, $\bar{q}_w$ and $\bar{\theta}_v$ at the same four times as in Fig. 2.7 for the case of the breaking stratocumulus deck in the upper half of the mixed layer.

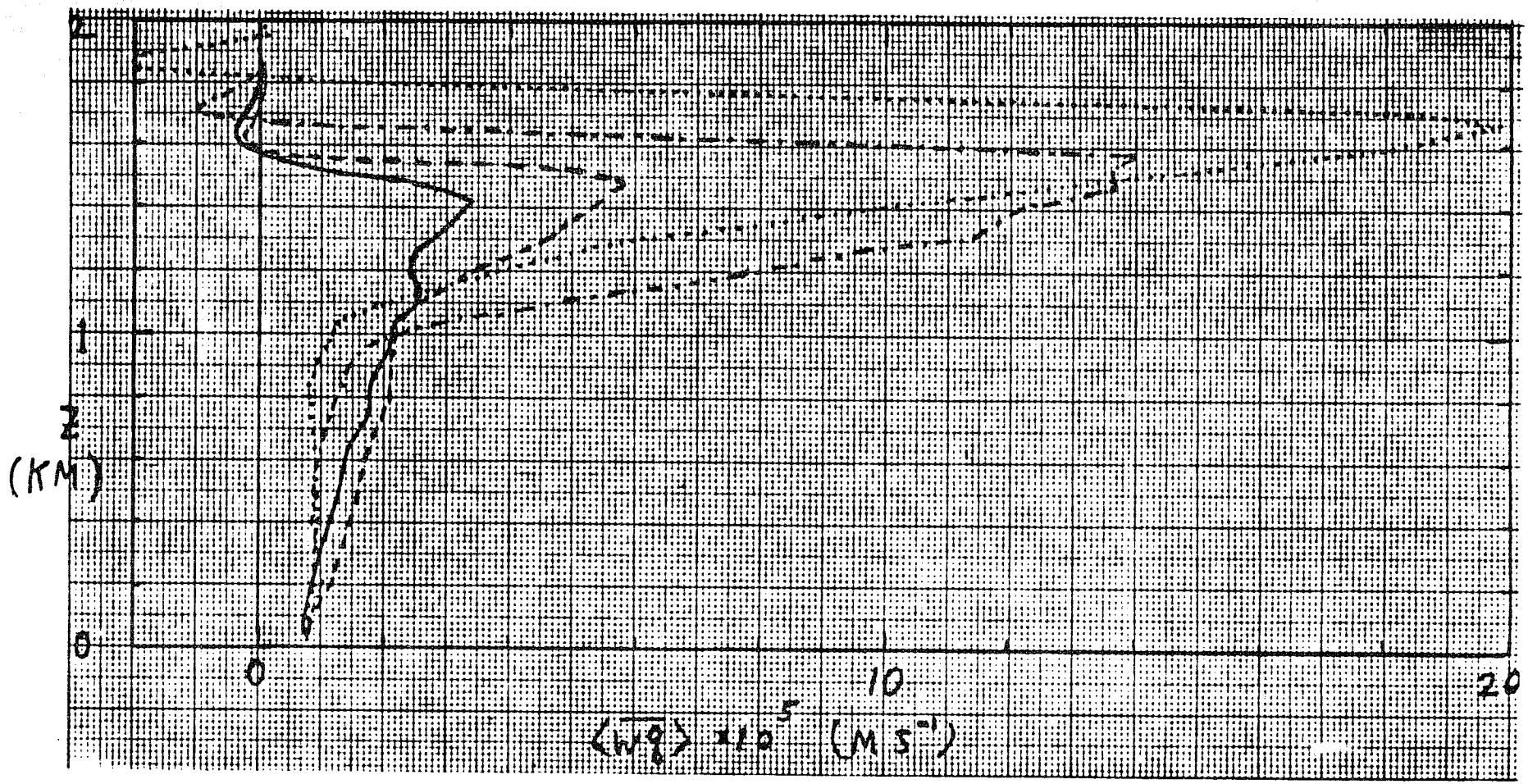

Fig. 2.9. Vertical profiles of moisture flux, $\langle \overline{wq_w} \rangle$, at the same four times as listed in Fig. 2.7, for the case of the breaking stratocumulus deck in the upper portion of the mixed layer.

since the thickness of the transition layer, $z_2 - z_1$, is always finite. In that case Eq (3.1) cannot be used, and we instead look at the equation describing the rate of development of $\Delta\theta_v$ (Tennekes, 1973):

$$\frac{d}{dt}\Delta\theta_v = w_e\left(\frac{\partial\theta_v}{\partial z}\right)^+ - \left[\langle w\theta_v\rangle_0 - \langle w\theta_v\rangle_h\right]/h$$

$$= w_e\left(\frac{\partial\theta_v}{\partial z}\right)^+ - (1+k)\langle w\theta_v\rangle_0/h \qquad (3.2)$$

If $\Delta\theta_v$ should indeed be vanishingly small for a significant period of time, it follows that $(d/dt)(\Delta\theta_v)$ is also small or negligible. Furthermore, in the absence of $\Delta\theta_v$ we expect to find little or no negative heat flux atop the mixed layer, so we set $k = 0$ in Eq (3.2). The resulting encroachment equation (see Carson and Smith, 1974) is

$$(w_e)_{enc} = \langle w\theta_v\rangle_0 / \left[h(\partial\theta_v/\partial z)^+\right] \qquad (3.3)$$

which would also become invalid if $(\partial\theta_v/\partial z)^+$ were vanishingly small.

3.1.3 Free entrainment. If $(\partial\theta_v/\partial z)^+ \to 0$ in Eq (3.3), we expect that the entrainment rate can proceed no faster than the rate at which turbulent vertical motions can carry mixed-layer air up into the quiescent air aloft. Even with $\Delta\theta_v \to 0$ and $(\partial\theta_v/\partial z)^+ \to 0$, this rate is finite and probably determined by the magnitude of the vertical motions within the mixed layer. With the assumption that $w_e \propto w_*$ in those circumstances, Deardorff (1974) found that

$$(w_e)_{free} = 0.2\, w_* \qquad (3.4)$$

where

$$w_* = \left(\frac{g}{\theta_v}\langle w\theta_v\rangle_0 h\right)^{1/3} \qquad (3.5)$$

is the convective velocity scale used in scaling the root-mean-square vertical motions (σ_w) in the mixed layer: i.e.,

$$\sigma_w / w_* = \text{Function}\,(z/h) \qquad (3.6)$$

Typically, w_* has a value between 1 and 2.5 m s^{-1}.

The circumstance of "free" entrainment can typically occur briefly around 10-11 AM over land when the mixed layer has warmed sufficiently to wipe out the stable jump and inversion layer associated with the previous night's cooling near the ground, and when the air aloft has an essentially neutral lapse rate left over from the previous afternoon's convective mixing. The free entrainment rate is sufficiently large, however, that the mixed layer spends very little time in this regime, and its top soon reaches a stable layer where encroachment first occurs, followed by forced entrainment after $\Delta\theta_v$ evolves.

3.1.4 Choice of entrainment formula. It is evident that neither the encroachment nor free-entrainment rate formula applies if a significant jump, $\Delta\theta_v$, exists. On the other hand, if $\Delta\theta_v$ becomes so small that $(w_e)_{forced}$ is predicted to exceed $(w_e)_{enc}$ the latter would apply unless it exceeded $(w_e)_{free}$ which is the maximum rate. Therefore a logical selection rule to apply is

$$w_e = \text{Minimum}\left[(w_e)_{forced}, (w_e)_{enc}, (w_e)_{free}\right] \qquad (3.7)$$

In other words, the criterion on when $\Delta\theta_v$ becomes too small for the forced-entrainment formula to apply is perhaps best framed by noting when $(w_e)_{forced}$ is predicted to exceed $(w_e)_{enc}$ or $(w_e)_{free}$.

3.2 The stratocumulus-capped mixed layer

As seen from Fig. 2.3, the vertical flux $\langle w\theta_v \rangle$ at $z = h$ (where it is usually negative) bears no particular relationship to $\langle w\theta_v \rangle_0$. The latter quantity could even be zero or slightly negative, with turbulence being supported by cloud top radiative cooling and/or the buoyancy flux in the cloud layer which depends upon cloud thickness. Yet, in order to close the jump condition at $z = z_1$ involving w_e, Eq (2.8a, b), a condition is needed involving a vertical flux at $z = z_1$ or at $z = h$. Most likely, this condition will relate $\langle w\theta_v \rangle_h$ in some way to the vertical integral of $\langle w\theta_v \rangle$ below $z = h$ or $z = z_1$. For this purpose, we need to relate $\langle w\theta_v \rangle$ to $\langle w\theta_e \rangle$ and $\langle wq_w \rangle$ both in the subcloud layer and in the cloud layer. In either case, we expect their profiles to be essentially linear with height up to $z = z_1$.

3.2.1 Formulation of $\langle w\theta_v \rangle$. From the approximate definition of θ_v in Eq (2.7), omitting overbars, we may obtain θ_v' and correlate with w' to obtain

$$\overline{w'\theta_v'} \cong (1 + 1.61\bar{q} - \bar{q}_w)\,\overline{w'\theta'} + 1.61\bar{\theta}\,\overline{w'q'} - \bar{\theta}\,\overline{w'q_w'} \tag{3.8}$$

where the overbar here represents any desired averaging. From the approximate definition of θ_e, we also find that

$$\overline{w'\theta'} = \overline{w'\theta_e'} - \left(\frac{L_v}{c_p}\frac{\theta}{T}\right)\overline{w'q'} \tag{3.9}$$

If the air is unsaturated, $\overline{w'q'} = \overline{w'q_w'}$ ($q = q_w$, $q_\ell = 0$) so that Eq (3.8) becomes

$$\overline{w'\theta_v'} = (1 + .61\bar{q}_w)\,\overline{w'\theta_e'} + \left[0.61\bar{\theta} - \frac{L_v}{c_p}\frac{\theta}{T}(1 + 0.61\bar{q}_w)\right]\overline{w'q_w'} \quad \text{(UNSATURATED)} \tag{3.10}$$

If the air is saturated ($q = q_s$, $q_\ell > 0$), however, we must make use of the approximate fluctuation form of the Clausius-Clapeyon equation

$$q_s' \approx 0.622\,\frac{L_v}{R\bar{T}}\,\frac{\bar{q}_s}{\bar{\theta}}\,\theta' \tag{3.11}$$

where R is the gas constant for air, to obtain, finally,

$$\overline{w'\theta_v'} = \left\{\left[1 + 1.61\bar{q}_s - \bar{q}_w + 1.61\left(\frac{0.62 L_v \bar{q}_s}{R\bar{T}}\right)\right] \Big/ \left[1 + \frac{0.62 L_v^2 \bar{q}_s}{R c_p \bar{T}^2}\right]\right\}\overline{w'\theta_e'} - \bar{\theta}\,\overline{w'q_w'}$$

$$= E_4\,\overline{w'\theta_e'} - \bar{\theta}\,\overline{w'q_w'} \quad \text{(SATURATED)} \tag{3.12}$$

From Eqs (3.10) and (3.12) the vertical integration of $\overline{w'\theta_v'}$ from the surface to $z = h$, assuming $(h - z_1) \ll h$, is straightforward though tedious. Neglecting radiative warming or cooling at cloud base or below, the result is (Deardorff, 1976):

$$I = \int_0^1 \overline{w'\theta_v'}\,d\,z/h = E_5(\overline{w'\theta'})_0 + E_6\bar{\theta}\,(\overline{w'q'})_0 + E_7\left(\frac{\theta}{T}\right)_1 \Delta R$$

$$- (E_7\,\Delta\theta_e - E_9\,\bar{\theta}\,\Delta q_w)(w_e)_{forced} \tag{3.13}$$

where E_5, E_6, E_7, E_9 are dimensionless functions of relative cloud thickness and make use of other constants ($E_1 \ldots E_4$) as specified below:

$$E_1 = 1 + 0.61\,\bar{q}_w$$

$$E_2 = [L_v/(c_p\bar{T})]\,E_1 - 0.61$$

$$E_3 = 0.62\,\frac{L_v}{R\bar{T}}\,\bar{q}_s \Big/ \left[1 + 0.62\,\frac{L_v}{R\bar{T}}\cdot\frac{L_v}{c_p\bar{T}}\,\bar{q}_s\right]$$

$$E_4 = E_1 - E_3\,(E_2 - 1)$$

$$E_5 = E_1\,\frac{z_c}{h}\left(1 - \tfrac{1}{2}\,\frac{z_c}{h}\right) + \tfrac{1}{2}\,E_4\left(1 - \frac{z_c}{h}\right)^2$$

$$E_6 = 0.61\,\frac{z_c}{h}\left(1 - \tfrac{1}{2}\,\frac{z_c}{h}\right) + \tfrac{1}{2}\,E_4\,\frac{L_v}{c_p\bar{T}}\left(1 - \frac{z_c}{h}\right)^2 - \tfrac{1}{2}\left(1 - \frac{z_c}{h}\right)^2$$

$$E_7 = \tfrac{1}{2}\left\{E_1\left(\frac{z_c}{h}\right)^2 + E_4\left[1 - \left(\frac{z_c}{h}\right)^2\right]\right\}$$

$$E_9 = \tfrac{1}{2}\,E_2\left(\frac{z_c}{h}\right)^2 + \tfrac{1}{2}\left[1 - \left(\frac{z_c}{h}\right)^2\right] \qquad (3.14)$$

The term involving $(w_e)_{forced}$ in Eq (3.13) appears because the vertical integrals of $\overline{w'\theta_e'}$ and $\overline{w'q_w'}$ required knowledge of the vertical fluxes at $z = z_1$ which involve $(w_e)_{forced}$ from Eqs (2.8). Values of the fluxes at the surface (subscript 0) are assumed known through use of bulk-aerodynamic heat and moisture transfer relations. Upon multiplying (2.8c) by E_4 and adding this to (2.8b) as multiplied by $\bar{\theta}$, one obtains the expression for $(\overline{w\theta_v})_h$ from (3.12):

$$(\overline{w\theta_v})_h = r\,E_4\,\Delta R - (w_e)_{forced}\left(E_4\,\Delta\theta_e - \bar{\theta}\,\Delta q_w\right) \qquad (3.15)$$

A closure assumption then applied to Eq (3.15) will relate the vertical buoyancy flux at $z = h$ to the integral I in (3.13), thus allowing w_e to be obtained.

3.2.2 Maximum entrainment condition. This assumption, first made by Ball (1960) for the unsaturated mixed layer, recognizes that the negative buoyancy flux associated with entrainment cannot be so large as to drive the integral I negative. If it were, there would be insufficient production of turbulence energy by buoyancy to support any dissipation at all within the mixed layer (neglecting the production due to wind shear which is often negligible above the surface layer). Then the assumption

$$I = 0 \qquad (3.16)$$

corresponds to this extreme limit, and allows a maximum value for $(w_e)_{forced}$ to be obtained from (3.13). Lilly (1968) tested this assumption on an episode of California coastal stratocumulus and found that the entrainment rate obtained was in reasonable balance with the estimated amount of large-scale subsidence at z = h. However, later studies of the turbulence energy balance for unsaturated mixed layers indicate that I $\sim$ 0.4 $(\overline{w\theta_v})_0$, and that I > 0 supports turbulence and energy cascade associated with a nearly constant rate of dissipation within the mixed layer above the surface layer. Fig. 2.5, shown earlier, suggests that the presence of stratocumulus enhances both the dissipation rate and the buoyancy flux. The maximum forced entrainment rate assumption also suffers from the inconsistency that if I = 0 there would be no way of generating the mixed-layer turbulence, in the vertical average, and in the absence of such turbulence there would be no entrainment.

3.2.3 Lilly's minimum entrainment rate. In order to estimate what might be a lower limit to w_e, and thereby bracket its estimate, Lilly (1968) postulated a minimum entrainment (greater than the trivial value of zero) can be obtained by setting $\langle\overline{w\theta_v}\rangle_h = 0$ in (3.12). Then a positive value of $(w_e)_{forced}$ occurs if $r\Delta R > 0$; i.e., if some of the cloud top radiative cooling occurs in the inversion layer. However, Lilly also assumed r = 1, so that the jump in $\overline{w'\theta_v'}$ between $z = z_1$ and z = h (see Fig. 2.3) was assumed non-existent. He further generalized this assumption to read

$$\overline{w'\theta_v'} = 0 \quad at \quad z = 0, \quad z = z_c, \quad or \quad z = h$$

$$\overline{w'\theta_v'} > 0 \quad elsewhere \quad (0 < z < h) \qquad (3.17)$$

Schubert (1976) has proposed that the actual forced entrainment rate be a weighted average of the maximum and minimum entrainment rates discussed above, such that proper results be obtained for the unsaturated mixed layer, for which the minimum rate is zero ($\Delta R = 0$).

The concept of the minimum entrainment rate for the stratocumulus capped mixed layer is untenable, however, upon realization that $\overline{w\theta_v}$ suffers a rapid decrease between $z = z_1$ and z = h, and that the parameter r in (3.15) is less than unity.

4. A revised entrainment-rate theory

4.1 Revised treatment of cloud top radiative cooling

The previous discussion points out how the cloud top radiative cooling may be partitioned between a fraction (r) which occurs within the inversion layer $h < z < z_2$, and the fraction (-r) within the upper mixed layer $z_1 < z < h$. The former fraction only indirectly causes mixed layer growth by cooling the cloud domes extending into the inversion layer, and thereby reducing the mean temperature at this mean height towards the mixed-layer temperature. The remaining fraction causes the jump in $\overline{w\theta_v}$ between z_1 and h, thereby tending to cool the entire mixed layer and at the same time create turbulence through the buoyancy force. Unfortunately, little is known about r; Deardorff (1976) assumed r = 0.5 in the absence of definitive information, while the numerical results later analyzed and discussed in section 2.2 suggest r ≈ 0.7.

4.2 Revised entrainment hypothesis

The revised hypothesis of Deardorff (1976) is that

$$(\overline{w\theta_v})_h = -0.5\,I \tag{4.1}$$

the right side of which becomes $-0.2(\overline{w\theta_v})_0$ for a cloud-free mixed layer. In this manner both the "minimum" and "maximum" entrainment hypotheses are avoided. However, as discussed in section 2.3, a hypothesis which is more reasonable in principle but would be much more complicated in practice relates the "negative area" to the "positive area":

$$\int_{z_1}^{z_2} \overline{w\theta_v}\, dz = -c' \int_0^{z_1} \overline{w\theta_v}\, dz$$

$$c''(\overline{w\theta_v})_h h = \quad " \tag{4.2}$$

where c' is of order 0.07, and c" is apparently of order 0.05 but probably depends upon the stability at z = h and upon the cloud opacity.

Combination of assumption (4.1) with (3.13) yields

$$(w_e)_{forced} = \left[E_5(\overline{w\theta})_0 + E_6\bar{\theta}(\overline{wq})_0 + 2rE_4\Delta R\right] / \left[(E_7+2E_4)\Delta\theta_e - (E_8+2)\bar{\theta}\Delta q_w\right] \tag{4.3}$$

where $E_5 \ldots E_9$ depend upon cloud thickness according to (4.13).

4.3 Comparison of theory with observations

4.3.1 California coastal stratus. Lilly (1968) examined the forced entrainment rate as obtained from the "maximum" and "minimum" assumptions from radiosonde soundings at Oakland, California, during an extended stratocumulus episode in August 1962, during which $h \simeq 620$ m, $z_c \simeq 345$ m, $\Delta\theta_e \simeq 5.7$ K, $\Delta q \simeq -4.8 \times 10^{-3}$, and $\Delta R \simeq 5.5$ cm s^{-1} K. For the "maximum" entrainment rate, he obtained 0.40 cm s^{-1} and for the minimum, 0.32 cm s^{-1}. The revised hypothesis of Eq (4.3) with r = 0.5 gives $(w_e)_{forced} = 0.38$ cm s^{-1}. The corresponding values of horizontal divergence (assumed constant with height) which would bring about a steady height, h, through the balance $w_e = -\bar{w}_h$ for h = 620 m, are, respectively, 6.5×10^{-6} s^{-1}, 5.2×10^{-6} s^{-1}, and 6.2×10^{-6} s^{-1}. Estimated values of the July mean surface divergence field just off the coast of north-central California range between 5 and 6×10^{-6} s^{-1}. All three hypotheses appear to have given reasonable estimates for w_e in this instance, with similar predictions apparently because the main source of turbulence was the cloud top radiative cooling rather than the surface heat or moisture fluxes.

4.3.2 Lake Michigan observations. Aircraft measurements of stratocumulus base and top heights, surface fluxes of heat and moisture, and mixed layer mean values were obtained by Lenschow (1973) from flights over the Great Lakes during cool-air outbreaks in the fall of 1970. The quantity dh/dt could therefore be deduced directly, but w_h was only poorly known; therefore w_e was also not known well. Nevertheless, for an assumed value of horizontal convergence which agrees with the mean of Lenschow's two estimates during passage of air over Lake Michigan, entrainment formula (4.3) with r = 0.5 in a simple one-dimensional model advecting with the speed of the mean wind yielded the w_e values shown in Fig. 4.1 as a function of downstream distance over the lake. Input values of surface θ (θ_{ss}) and surface q (q_{ss}) are also shown, along with the calculated values of lower mixed-layer θ (θ_m) and q_w (q_{wm}). The mean wind near the surface was taken to be 11 m s^{-1}, the mean wind in the same direction averaged over the mixed layer was taken as 8 m s^{-1}, and ΔR was taken as 6.0 cm s^{-1}K, all from Lenschow's data. From the model deductions of θ_m and q_{wm}, a lifting-condensation level cloud base (z_c) could also be deduced, and the comparison

between the calculated and observed curves of h and z_c is shown in the lower portion of the figure. If the effects of entrainment had been omitted, there would have been no semblence of agreement with observations.

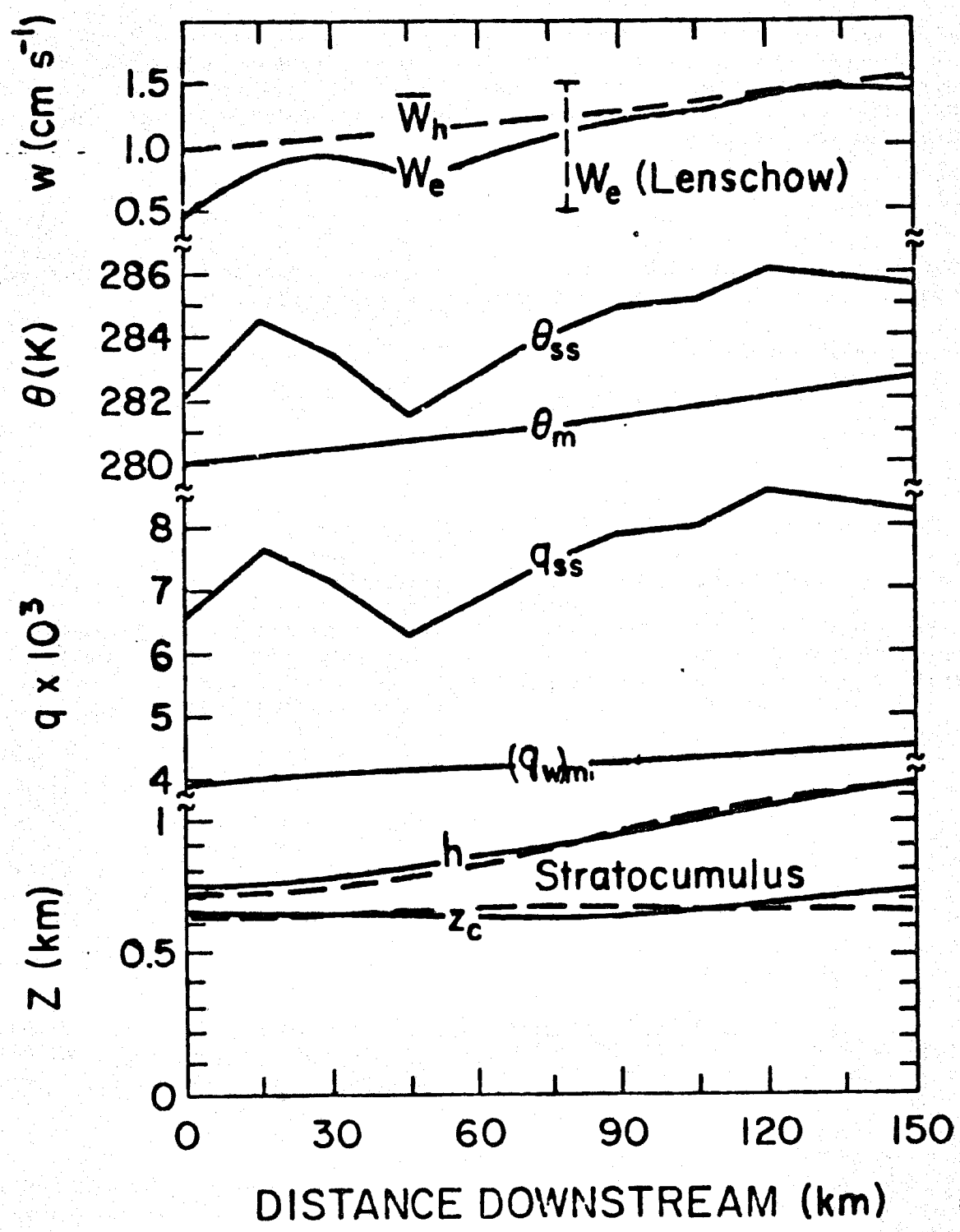

Fig. 4.1. One-dimensional model calculations, using Eq(4.3), of entrainment rate, h, cloud base (z_c), mixed-layer θ, and mixed-layer q_w, for the case of cool-air flow downstream over Lake Michigan in November, 1970. Initial conditions, surface potential temperature (θ_{ss}), q_s at the water surface (q_{ss}) and radiative flux divergences are taken from Lenschow (1973). Lenschow's two estimates of w_e are denoted by the ends of the dashed bracket. Figure is from Deardorff (1976b).

4.3.3 AMTEX observations. As of this writing the few AMTEX observations of 1974 which have been analyzed were accompanied by broken stratocumulus with about 75% coverage. Entrainment theories have not yet been developed for the broken stratocumulus case, and it is a rather crude assumption to interpolate between predicted values for the totally saturated case and the clear case according to the estimated cloud fraction. The value of $\Delta\theta_e$ associated with the broken stratocumulus was in the range -0.5 K to -2.0 K. Application of Eq (4.3) yielded $(w_e)_{forced} \simeq 8$ cm s^{-1}. It was observed that $dh/dt \simeq 0$, meaning that $-w_h \simeq w_e$ while an estimate of w_h from the nearest triangle of radiosonde wind measurements was -5 cm s^{-1}. Hence, entrainment formula (4.3) overpredicted w_e by a factor of about 1.6 in this case, suggesting increasing inaccuracy as $\Delta\theta_e$ becomes negative. However, the theory also needs extension to the breaking stratocumulus case.

4.4 Stratocumulus encroachment and free entrainment.

Is there an encroachment formula for the case of stratocumulus, corresponding to that for the unsaturated case in which $\Delta\theta_v \to 0$?

First, we may rewrite (3.12) to read

$$w_e = \left[r E_4 \Delta R - (\overline{w'\theta_v'})_h \right] / \left[E_4 \Delta\theta_e - \bar{\theta} \Delta q_w \right]$$

(SATURATED) (4.4a)

in analogy to

$$w_e = -(\overline{w'\theta_v'})_h / \Delta\theta_v$$

(UNSATURATED) (4.4b)
(and no cumulus)

discussed earlier.

In the case of encroachment when the thermal jump approaches zero, we expect the negative buoyancy flux of entrainment to approach zero also. For the unsaturated mixed layer, (4.4b) properly reduced to an indeterminate ratio in this case, and the concept that $\Delta\theta_v$ and $(\partial/\partial z)\Delta\theta_v$ be zero supplies the encroachment condition, (3.3). For the saturated upper mixed layer, (4.4a) does not similarly become indeterminate as the thermal stability jump, $E_4\Delta\theta_e - \bar{\theta}\Delta q_w$ approaches zero, because of the term $rE_4\Delta R$ in the numerator which is generally positive. This result indirectly suggests that encroachment is not possible for the stratocumulus-capped mixed layer.

Second, is the denominator of (4.4a) the thermal jump which becomes vanishingly small for encroachment to occur, or is it the different denominator of (4.3)?

Third, in analogy to the clear mixed layer, we would require that encroachment for the cloud-capped boundary layer be accompanied by well mixed profiles of conservative properties, and linear vertical fluxes. However, we saw in Figs. 2.8 and 2.9 that the entrainment rate is sufficiently rapid when $\Delta\theta_e$ is slightly negative that these conditions are no longer met, and the cloud deck cannot remain solidly saturated.

For these reasons there is not yet any generally recommended encroachment formula for the cloud-capped mixed layer.

In deriving a maximum entrainment rate associated with free entrainment, in analogy to Eq (3.4), we notice that the free-convection velocity scale w_* needs generalizing to account for buoyancy production associated with upward moisture flux in the cloud layer, and cloud top radiative cooling. We also note that (3.5) could be rewritten

$$w_* = \left(2 \frac{g}{\bar{\theta}_v} I h \right)^{1/3} \tag{4.5}$$

where I is the vertical integral of (3.13), if there were no buoyancy flux atop the mixed layer. If we again assume that the entrainment can proceed no faster than 0.2 w_*, and make use of Eq (3.13) for I with the term involving $(E_7 \Delta\theta_e - E_9 \bar{\theta} \Delta q_w)$ neglected on the grounds that this stability jump will be very small then, we obtain the free-entrainment formula

$$(w_e)_{free} = 0.25 \left\{ \frac{g}{\bar{\theta}_v} h \left[E_5 (\overline{w\theta})_0 + E_6 \bar{\theta} (\overline{wq})_0 + E_7 \Delta R \right] \right\}^{1/3} \tag{4.6}$$

for the cloud-capped case.

Although the assumptions leading to (4.6) are again believed to become invalid as the entrainment rate becomes very rapid, (4.6) supplies an upper limit to w_e of order 40 cm s^{-1}. Hence, in analogy to Eq (3.4), Deardorff (1976) recommended

$$w_e = \text{Minimum} \left[(w_e)_{forced} , \ (w_e)_{free} \right] \tag{4.7}$$

oud-capped mixed layer, with $(w_e)_{forced}$ given by (4.3) and $(w_e)_{free}$ .6).

tered cumulus atop the mixed layer

Soon after theories began appearing on the growth rate of the clear mixed layer in the late sixties and the early seventies, it became apparent that important modifications were necessary to take into account the occurrence of scattered cumuli growing out of the top of the mixed layer. Whenever such cumuli display vertical development associated with release of latent heat, it is evident that they are extracting air from the mixed layer and, for the most part, leaving this air later within a "cloud layer" lying above the mixed layer. During the short period of time that any developing cumulus is siphoning air out of the mixed layer, it is evident that it is providing compensating downdraughts of clear air at cloud-base height, in fulfillment of the continuity equation. If the developing cloud is tall, these compensating downdraughts, known as cloud-induced subsidence, are believed to extend outwardly to distances comparable to the developing cloud's height. There they are indistinguishable from large-scale subsidence as far as the underlying mixed layer is concerned. We therefore expect that an additional, cloud-induced subsidence term (w_{cs}) should appear in the mixed-layer growth equation in these circumstances:

$$\frac{dh}{dt} = w_e + \bar{w}_h - w_{cs} \tag{5.1}$$

which could allow h to reach a steady value even in the absence of large-scale subsidence, $-w_h$. (The quantity w_{cs} is here defined to be positive.)

5.1 Localized cloud-induced subsidence

It is of interest to explore the w_{cs} term in (5.1) by examining Lilly's (1968) jump relations in this instance. We again integrate the equation for a conservative thermodynamic variable (θ_ℓ, say) and conservative moisture variable, q_w, from just below $z = h$ to a height just above, (z_2), which includes cloud-base height. We now ignore cloud-top radiative cooling because the cloud tops extend above $z = z_2$ and because the cloud fraction is presumed to be relatively small. The results, similar to (2.8a) and (2.8b), are

$$(\overline{w\theta_\ell})_1 = (\overline{w\theta_\ell})_2 - w_e \Delta\theta_\ell \tag{5.2a}$$

$$(\overline{wq_w})_1 = (\overline{wq_w})_2 - w_e \Delta q_w \tag{5.2b}$$

where it is again presumed that jumps $\Delta\theta_\ell$ and Δq_w exist, centered at $z = h$ ($z_1 < h < z_2$). These equations now differ from the earlier ones in that the fluxes at $z = z_2$ are no longer negligible but are finite because of the presence of scattered cumulus extending upwards from about this height. The simplest parameterization of these fluxes is

$$(\overline{w\theta_\ell})_2 = -c\,\sigma_c\, w_{cb}\, \Delta\theta_\ell \tag{5.3a}$$

$$(\overline{wq_w})_2 = -c\,\sigma_c\, w_{cb}\, \Delta q_w \tag{5.3b}$$

where w_{cb} is a cloud-base in-cloud mean vertical velocity, σ_c is the cloud fraction existing at cloud-base height (or at $z = z_2$), and c is a constant. If σ_c is small, the product $c\sigma_c w_{cb}$ will be shown to be the effective cloud-induced subsidence:

$$c\sigma_c w_{cb} = w_{cs} \tag{5.4}$$

where w_{cs} is also known as the cloud mass flux at cloud-base height.

The parameterization of (5.3) has been used by many authors (e.g., Ogura and Cho, 1974). The rationale is that

$$\Delta\theta_\ell \approx (\theta_\ell)_{cloud} - (\theta_\ell)_{envir.} \approx (\theta_\ell)_{mixed\ lyr.} - (\theta_\ell)_2 \tag{5.5a}$$

$$\Delta q_w \approx (q_w)_{cloud} - (q_w)_{envir.} \approx (q_w)_{mixed\ lyr.} - (q_w)_2 \tag{5.5b}$$

since the cloud is starting out with properties of the mixed layer and, at cloud-base height, is surrounded by "environmental" air having mean properties at $z = z_2$ for a small cloud fraction.

Next, we wish to combine (5.2a) and (5.2b) in such a manner as to obtain an equation for $(\overline{w\theta_v})_1$:

$$(\overline{w\theta_v})_1 = (1 + 0.61\bar{q})(\overline{w\theta_\ell})_1 + 0.61\bar{\theta}\,(\overline{wq_w})_1 \tag{5.6}$$

The result, upon making use of (5.2) and (5.3), is

$$(\overline{w\theta_v})_1 = -(w_e + c\sigma_c w_{cb})\left[(1+0.61\bar{q})\Delta\theta_\ell + 0.61\bar{\theta}\,\Delta q_w\right] \tag{5.7}$$

Finally, a closure assumption is again needed for $(\overline{w\theta_v})_1$. The study of Sommeria (1976) indicates that

$$(\overline{w\theta_v})_1 = -k(\overline{w\theta_v})_0 \qquad (k \approx 0.2) \tag{5.8}$$

still holds in the presence of a layer of scattered cumulus, although this is contested by Esbensen (1975) when the overbar represents a large-scale, several-day average. Both results may be correct, with (5.8) holding over a local quasi-homogeneous region but not over an area so large that h and cloud-base height vary by a factor of 1.5 or more.

Upon inserting (5.8) into (5.7) we obtain

$$\frac{dh}{dt} - \bar{w}_h = -c\sigma_c w_{cb} + k(\overline{w\theta_v})_0 \Big/ [(1+0.61\bar{q})\Delta\theta_l + 0.61\bar{\theta}\Delta q_w]$$

$$= -w_{cs} + k(\overline{w\theta_v})_0 / \Delta\theta_v \tag{5.9}$$

The last term on the right is the entrainment rate associated with surface-induced mixed-layer turbulence, while w_{cs} is the counteracting (negative) entrainment rate associated with cloud turbulence. If we identify the symbol w_e with only the right-hand term, then we obtain Eq (5.1).

Given a parameterization for the cloud-base mass flux, w_{cs}, we do not need to know the constant c in Eq (5.9). The purpose in introducing this constant is to emphasize that w_{cs} may only be proportional to the product of actual cloud-fraction and actual cloud-mean vertical velocity near cloud-base height, not equal to it. Three-dimensional numerical studies (as in Sommeria, 1976) and aircraft measurements (as in GATE) are each on the verge of being able to supply values of σ_c and w_{cb}, as well as the fluxes in Eq (5.3), which would allow evaluation of the constant c. This would then permit development of a parameterization of w_{cs} which is based upon σ_c at cloud-base height as in Eq (5.9).

A preliminary parameterization for w_{cs} being developed at NCAR does not yet incorporate a comprehensive parameterization of cloud mass flux. This parameterization for the cloud-induced subsidence at z = h is:

$$w_{cs} = 1.65\,\sigma_c(1-\sigma_c)\,w_* \Big/ \left\{1 + 0.167\frac{g}{\bar{\theta}_v}h\left[\Delta\theta_v + 0.1h\left(\frac{\partial\theta_v}{\partial z}\right)^+\right] / w_*^2\right\} \tag{5.10}$$

This formulation is designed to give zero cloud mass flux for no clouds or for solid stratocumulus, and to give an increased cloud mass flux for decreased stability atop the mixed layer (small $\Delta\theta_v$ and small value of $(d\theta_v dz)^+$ aloft). The constant, 1.65, was obtained by Benoit (1976) by testing a time-dependent mixed-layer model against ATEX data of Augstein et al. (1974) in which σ_c was of order 2 to 4%, w_* of order 0.7 m s^{-1}, $\Delta\theta_v$ of order 0.1 K, $(\partial\theta_v/\partial z)^+ \simeq 4.6$ K/km, and $h \simeq 700$ m.

5.2 Cloud-induced fluxes atop the mixed layer

Some of these have already been expressed in Eq (5.3). With the inclusion of momentum fluxes similarly, they are

$$(\overline{w\theta_l})_2 = -w_{cs}\Delta\theta_l \qquad (\overline{uw})_2 = -w_{cs}\Delta u$$

$$(\overline{wq_w})_2 = -w_{cs}\Delta q_w \qquad (\overline{vw})_2 = -w_{cs}\Delta v \tag{5.11}$$

Thus, a parameterization which requires the momentum flux just below the level z = h, $(\overline{uw})_1$, in order to help predict the mean wind speed within the mixed layer, would utilize

$$(\overline{uw})_1 = (\overline{uw})_2 - w_{cs}\,\Delta u \tag{5.12}$$

5.3 Prediction of cumulus cloud fraction

One must first have an estimate of σ_c before one knows whether to apply a mixed-layer entrainment formula derived for scattered cumulus, one for stratocumulus, or some hybrid mixture. Assuming that estimates of both the mixed-layer height, h, and lifting condensation level, LCL, are available, Benoit (1976) has proposed that σ_c be diagnosed by

$$\sigma_c = \left[\frac{1}{(LCL/h) - 0.37} - 0.88\right]^2 \tag{5.13}$$

This prescription simulates no cumulus clouds if LCL > 1.5 h, about 0.5 cloud cover for LCL = h, and solid stratocumulus for LCL $\leq$ .9 h. Although most observations within a local, relatively homogeneous region suggests that $\sigma_c = 0$ for LCL > 1.15 h, the latter fraction of h must increase as the grid area becomes larger. The exponent 2 in (5.13) simulates a small probability of occurrence of broken stratocumulus in comparison with scattered cumulus, for equally probable values of LCL/h.

The attempted diagnosis of boundary-layer cloud fraction in this section thus serves three functions:

(a) to permit a cloud-induced subsidence to be estimated for the purpose of calculating a mixed-layer growth rate;

(b) to permit estimates of the vertical fluxes at cloud-base height which one needs in estimating these fluxes just below z = h;

(c) for purposes of estimating the cloud-blockage effect upon solar radiation and outgoing long wave radiation at the ground surface, and in calculating radiative flux divergences at GCM height levels.

5.4 Transition from stratocumulus to scattered cumulus

The usual mode of this transition, over land, is for the LCL to rise faster than does h, due to the influence of surface heating in lifting the LCL (typical example: the dissipation of morning stratocumulus in the Los Angeles basin). The described parameterization for σ_c includes not only this mode of transition, but also a second possibility that h may move downward faster than does the LCL, thereby also causing a simulated stratocumulus deck to change to cumulus and then perhaps to clear skies.

A transition mode about which much less is known, however, occurs typically over the ocean: the transition from stratocumulus with base at $z = z_c$ and top at z = h, to scattered cumulus with bases at z_c (just above the new h) and tops at the previous h. As seen in section 2.4, this appears to occur when the entrainment rate is so rapid that the "mixed" layer turbulence cannot maintain a well mixed layer of solid saturation. A rough measure of the onset of this condition, when $\sigma_c = 1$, is $w_e/w_* > 0.06$, and this has been generalized by Benoit (1976) to

$$w_e/w_* > \left[0.06\,\sigma_c + 0.2\,(1 - \sigma_c)\right] \quad \text{(for transition)} \tag{5.14}$$

where w_* is given by (4.5). If (5.14) is satisfied and stratocumulus is present within a boundary layer parameterization, then h can be prescribed to decrease by a certain fraction per time step of a GCM calculation to simulate this transition. The proper rate of decrease is as yet unknown, however.

A fourth mode of dissipation of stratocumulus is when it loses all contact with the boundary-layer turbulence, in which case it slowly evaporates. This occurs when the boundary layer switches from unstable to stable (the integral I becomes negative). The crudest possible parameterization of this process is to decrease σ_c at a prescribed rate when $I < 0$, which requires that a past value of σ_c be stored at each grid point of the parameterization.

Unless all four dissipative mechanisms mentioned above are included, a parameterization for σ_c within a long-term numerical integration is likely to end up with far too much simulated stratocumulus clouds over the globe.

6. Preliminary results of applying a comprehensive boundary-layer parameterization to one of NCAR's global circulation models

6.1 Main elements of the parameterization

The parameterization was developed initially for use in the NCAR six-layer GCM with 5° latitude and longitude resolution. The model includes smoothed orography and specified ocean surface temperatures. The vertical coordinate is simply z and the first level above sea level at which winds, temperature, and humidity are calculated is 1.5 km; the first level for $\bar{w}$ is 3 km; the next level for winds is 4.5 km, etc. This model is described by Washington (1974).

A ten-day comparison run was made with this GCM using the standard versus the parameterized-BL version. It was started at DAY 60 (60 days after a start-up from an atmosphere at rest) for a date in January. The main elements, described in detail in the Ph.D. thesis of R. Benoit (1976) are:

(a) Surface fluxes related to surface-to-air differences and roughness length by the use of Monin-Obukhov empirical similarity theory. The roughness length was set at 20 cm over land and .25 mm over water. A rigorous treatment of free convection is made. The standard NCAR GCM utilized constant coefficients of drag, heat and moisture transfer, with a drag coefficient of .003 over both land and sea. It also utilized "contact layer" values for surface-layer properties, derived in a manner which placed these values intermediate between surface values and 1.5 km values. The "contact-layer" wind had the same direction as the wind at 1.5 km, and its magnitude was not permitted to drop below 5 ms^{-1}.

(b) Prediction of entrainment rate, h, and cloud fraction as outlined in sections 3-5; the standard GCM estimated cloud fraction at the heights 3 km and 9 km, and did not attempt any prediction of h.

(c) Time-dependent prediction of mean wind velocity, potential temperature and specific umidity at a height of 10 m above the surface. These values are then used in the diagnosis of the surface fluxes.

(d) Diagnosis of the vertical gradients of stress, heat flux and moisture flux for use at the 10 m height. These are used in the previous step (c) and constitute an exploratory part of the parameterization. The parameterized flux gradients involve a surface flux, the flux just below z = h, and the height h. The stress gradients include also the influence of mean baroclinicity within the BL, mean wind shear, fh/u_* and cross-isobaric wind angle.

(e) Diagnosis of jumps in variables across z = h by upward extrapolation from the 10 m value and downward from GCM values above h. The inherent limitations of a parameterization for a GCM having coarse vertical resolution is strongly evident in this step. Often this step yielded $\Delta\theta_v < 0$, in which case $\Delta\theta_v$ was set to zero by adjustment of $\Delta\theta$. At other times and locations $\Delta q > 0$; this seems to occur more often in the model than is expected in Nature.

(f) Calculation of ground temperature over land using a surface energy balance in which the soil heat flux is obtained explicitly. This involves the solution for soil temperature within six layers of increasing thickness with increasing depth. The layers move up and down with the occurrence of snowfall or snow melt. The standard GCM utilized a surface-energy balance in which the soil heat-flux term is assumed to be one-third of the sensible heat flux. The treatment of soil moisture was not changed, with a net soil moisture content gradually being altered according to the value of precipitation plus snow melt minus evaporation. The evaporation rate at the bare ground surface was related to its potential evaporation value according to the degree of mean-soil wetness.

6.2 Examples of evolution of surface-layer properties and h

6.2.1 At a fair weather land location. The evolution of h, the LCL, and w_e from the BL version during DAY 66 at a location in SE Australia is shown in Fig. 6.1. The boundary-layer height reaches about 2.7 km by late afternoon and drops to a few hundred meters at night. However, the dropoff is quite gradual because of difficulties previously encountered when an abrupt drop to 50 m had been programmed to occur as the surface layer switches from unstable to stable. A rapid growth of h occurs for one and one-half hours shortly after sunrise, associated with the absence then of a positive jump, $\Delta\theta_v$, at z = h, and nearly adiabatic conditions aloft. This premature situation soon remedies itself when the growth of h later led to diagnosis of a positive jump, $\Delta\theta_v$. The subsequent growth of h during the day is very reasonable. No clouds occur because the LCL remains well above h; the LCL grows during midday at about the same rate that h does because of drying and warming of the boundary layer. The moisture fluxes at z = 0 and at $z = z_1$ (just below h) responsible for this drying are shown in Fig. 6.2, along with u_*^2 and the sensible heat flux. In this instance Δq was negative, and the entrainment rate is sufficiently large to cause $(\overline{wq})_1$ to exceed $(wq)_0$.

The sensible heat flux varies as expected, reaching a (summertime) maximum of .39 m s^{-1} K around noon, in contrast to a value less negative than -.05 m s^{-1} K the previous night. The small values of u_*^2 at night are also realistic.

Soil temperatures (not shown) also varied reasonably. The ground temperature reached a minimum of 295 K at sunrise and a maximum of 318 K at 2-3 p.m. Sub-soil temperatures displayed progressively less diurnal amplitude and greater phase lag. A parameterization which either ignores the soil heat flux, or sets

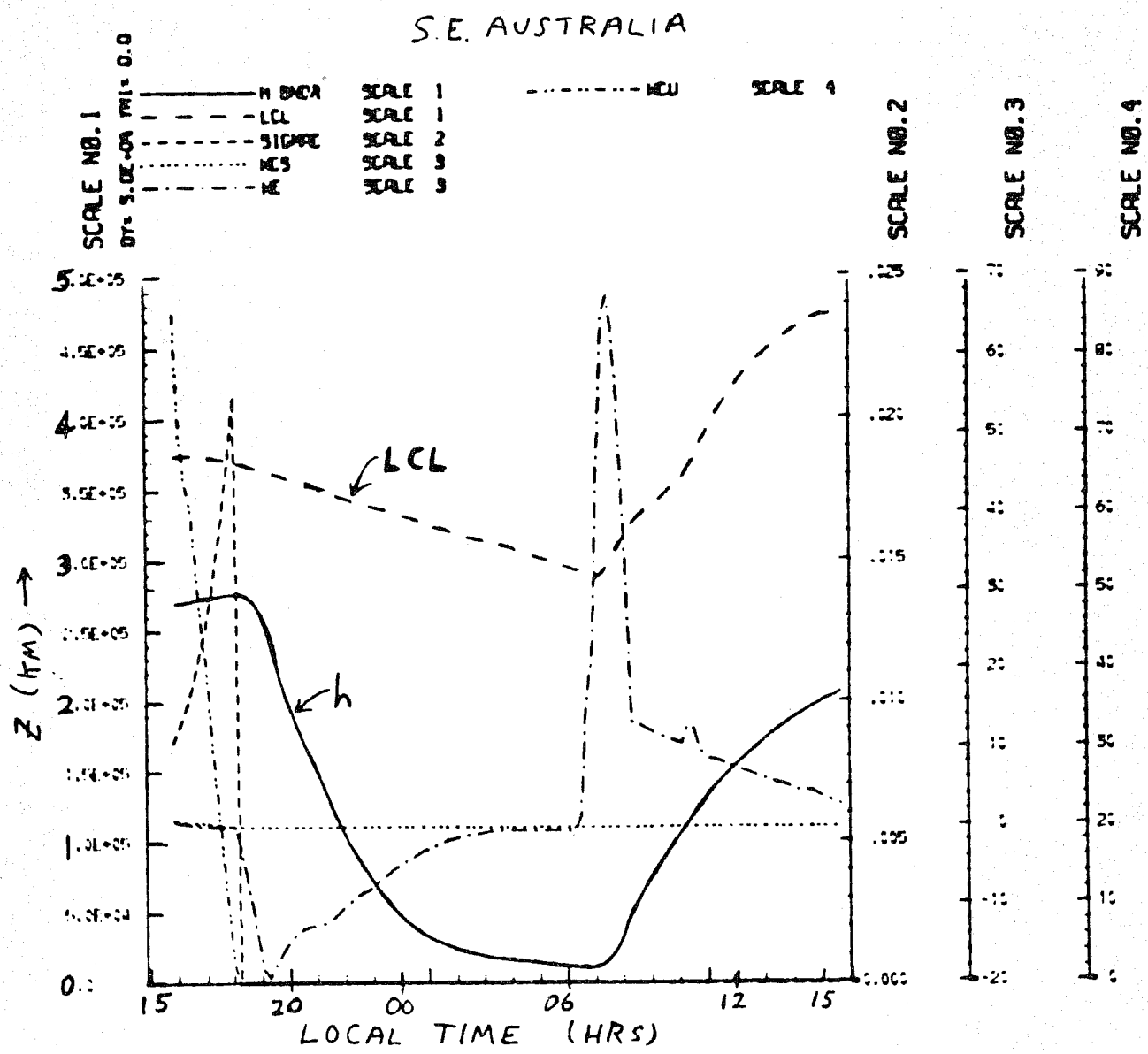

Fig. 6.1. Calculated evolution of h, the LCL and other properties during a 24-hr period at a grid point located in SE Australia during DAY 66 within t NCAR GCM version with the BL parameterization.

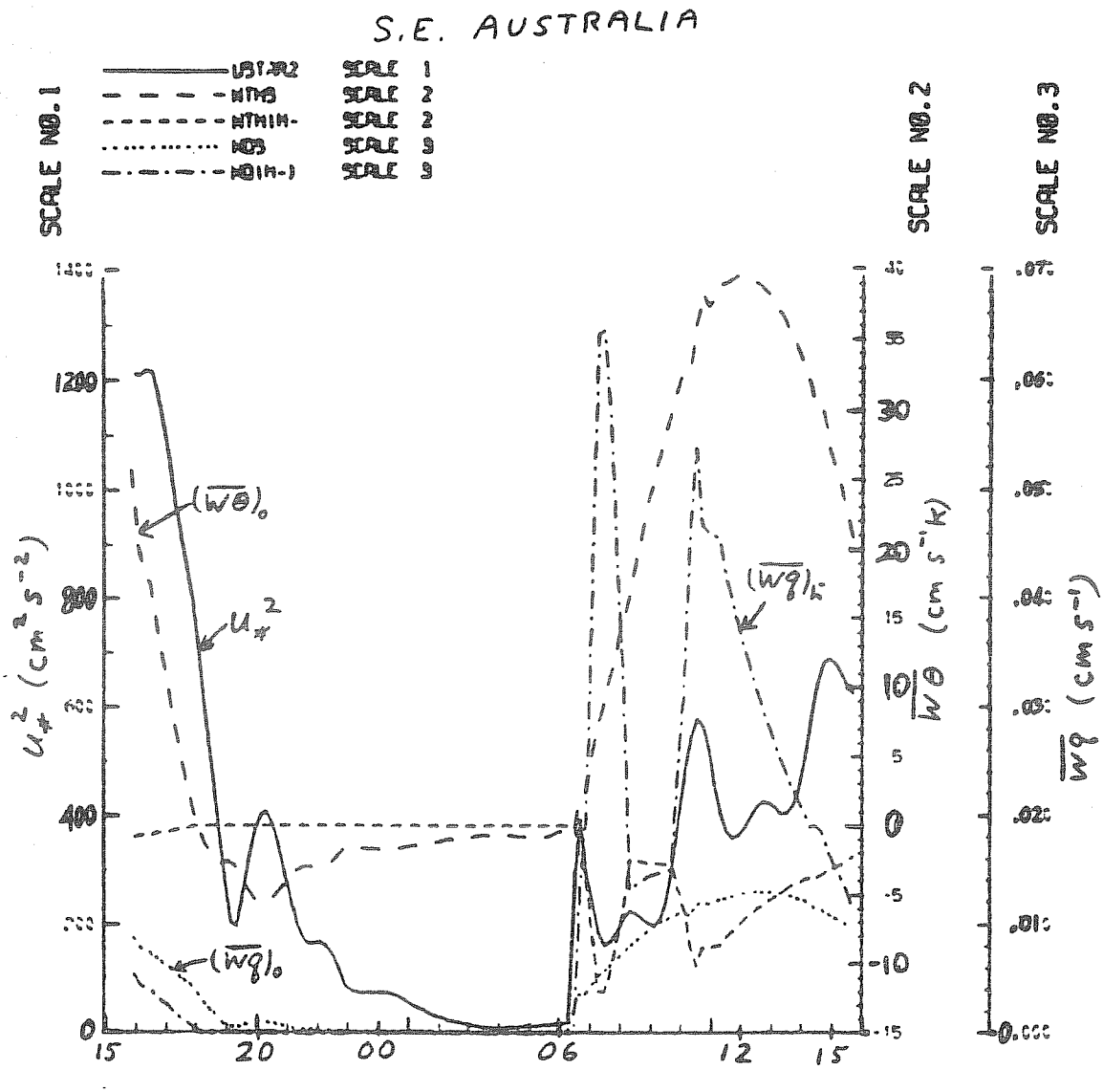

Fig. 6.2. Calculated evolution of u_*^2, $(\overline{w\theta})_o$, $(\overline{wq})_o$ and $(\overline{wq})_h$ during a 24-hr period at a grid point located in SE Australia during DAY 66.

it equal to a fraction of the sensible heat flux, tends to predict the maximum ground temperature to occur too close to noon.

6.2.2 At a fair weather oceanic location. At a location close to Puerto Rico (considered an ocean grid point in the GCM) the evolution of h, the LCL, σ_c and w_e during DAY 66 are shown in Fig. 6.3. h varies between 500 and 600 m, in quasi-equilibrium with cloud-induced subsidence associated with σ_c varying between 2 and 3%. Associated values of cloud-induced subsidence (w_{cs} in Eq. 5.9) ranged between 0.5 and 1.5 cm s^{-1}.

Values of the surface fluxes and those occurring just below z = h are shown in Fig. 6.4. The heating due to convergence of the sensible heat flux in the mixed layer is counteracted by radiative and advective cooling; the slight moistening due to the slight convergence of the moisture flux tends to be offset by advection of drier air from the northeast. The wind velocity at $z = z_a$ became very weak during the middle of this day ($u_a \sim$ 2-3 m s^{-1}), and all the surface fluxes reflect this. This weak wind was associated with a rather weak surface pressure gradient of erratic direction. A shortcoming of the GCM which this kind of examination has revealed is the usual existence of 2-3 hr oscillatio in the surface geostrophic wind of amplitude about 4 m s^{-1}. These are believed to be manifestations of inertial-gravity waves possibly triggered by occasional releases of latent heat within the standard GCM cloud precipitation parameterization utilized.

At other locations around the globe stratocumulus sometimes occurred, and the evolution of h, the LCL, and σ_c was then often much more erratic than in the examples shown. Work is continuing to improve the associated assumptions of the parameterization to remove such non-physical effects.

6.3 Global fields of h and of σ_c

Global fields of h in the Western Hemisphere, Fig. 6.5, and in the Eastern Hemisphere, Fig. 6.6, on DAY 66 at 0600 Greenwich time exhibit rather uniform values over the oceans ranging mostly between 300 and 700 m. It is nighttime in North and South America where h is generally less than 400 m (height above the ground), and afternoon in Asia and Australia where h has reached the vicinity of 2 km or somewhat more. Other values of large h over the Yucatan Peninsula, South Africa, the Mackenzie Bay, and New Zealand are regions of low pressure or strong cyclonic curvature of the surface isobars. A few isolated packets of very large h (6 km above sea level--they appear as black smudges) occur near the edges of Greenland, Antarctica and the northern Himalayas, and are believed caused spuriously by an improper parameterization of the effects of large (terrain induced) baroclinicity as it affects the surface-layer wind, u_*, and finally w_e.

Figures 6.7 and 6.8 of the boundary layer cloud fraction, σ_c, generally show an absence of cloudiness over those continents which are experiencing nighttime, and also over dry Australia. Over the oceans the BL cloudiness is usually predicted to be less than 4%. Exceptions frequently occur over low-pressure areas, and some of the high pressure areas over land at night are also predicted to be overcast with stratocumulus. Relatively large amounts of stratocumulus are also predicted to occur over Antarctica. It is not predicted to occur off the west coast of California, Peru, and Angola; these are found

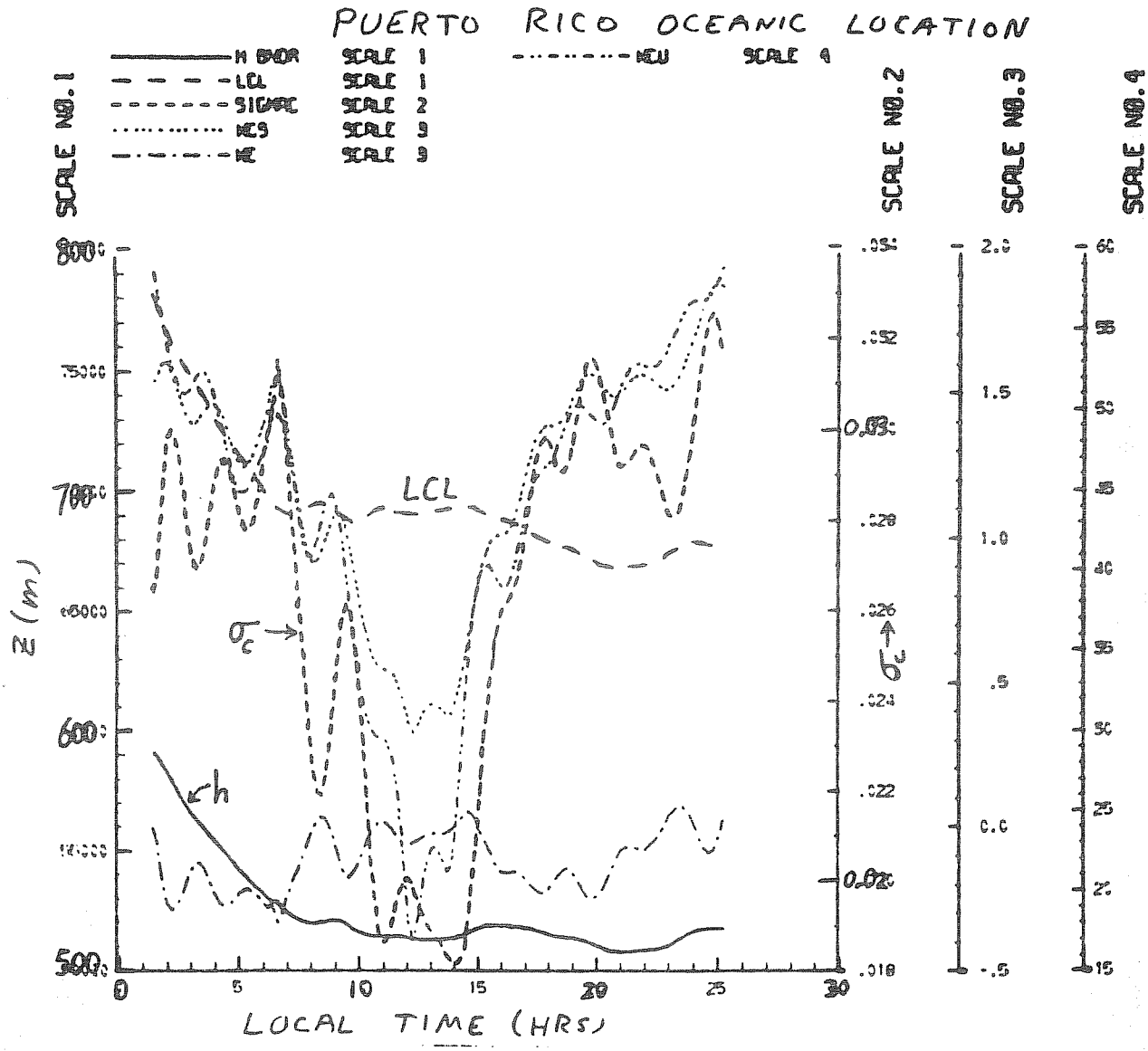

Fig. 6.3. Calculated evolution of h, the LCL, σ_ε and other quantities during a 24-hr period at an oceanic grid point near Puerto Rico during DAY 66.

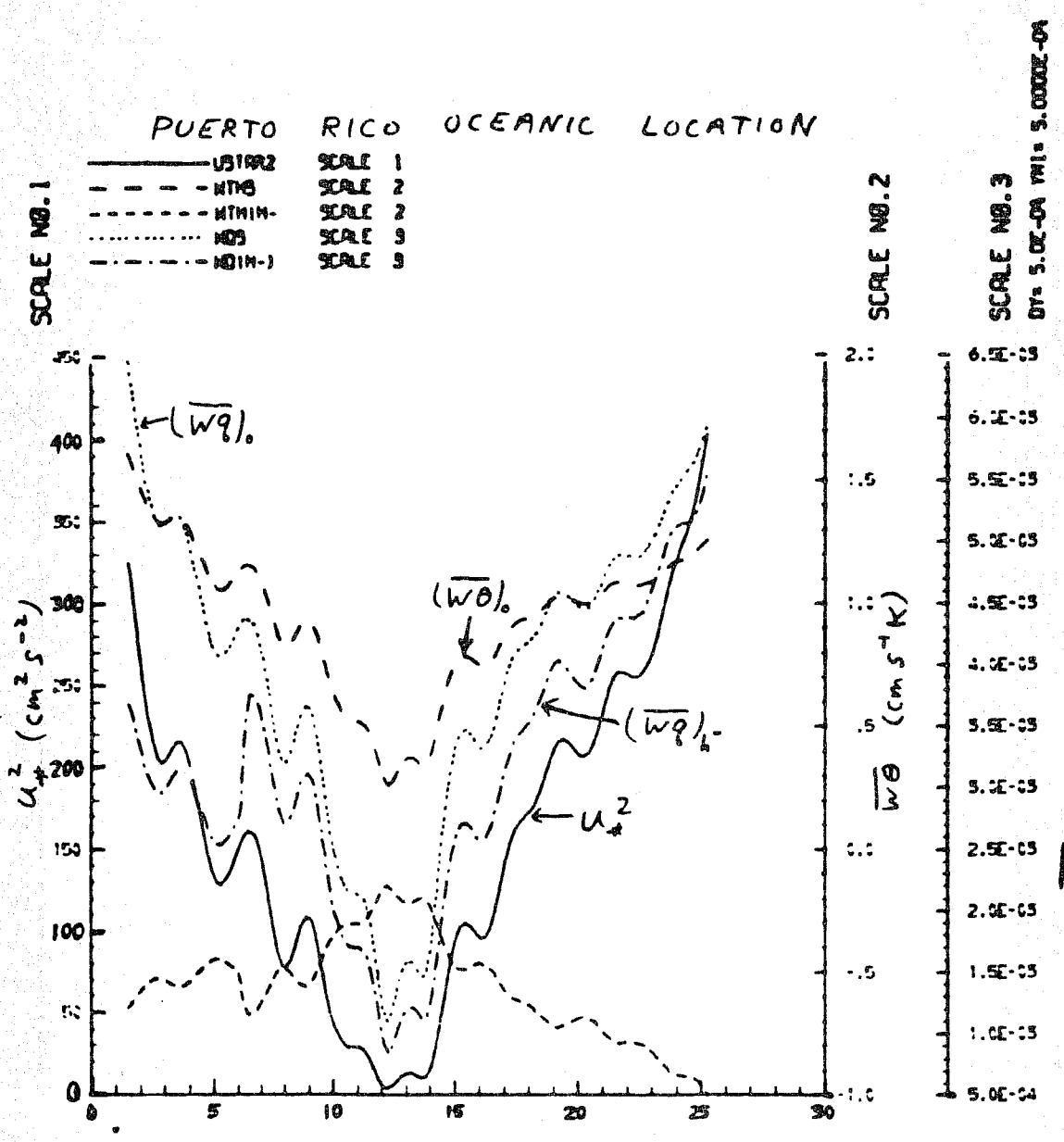

Fig. 6.4. Calculated evolution of u_*^2, $(\overline{w\theta})_o$, $(\overline{wq})_o$ and $(\overline{wq})_h$ during a 24-hr period at an oceanic location near Puerto Rico during DAY 66.

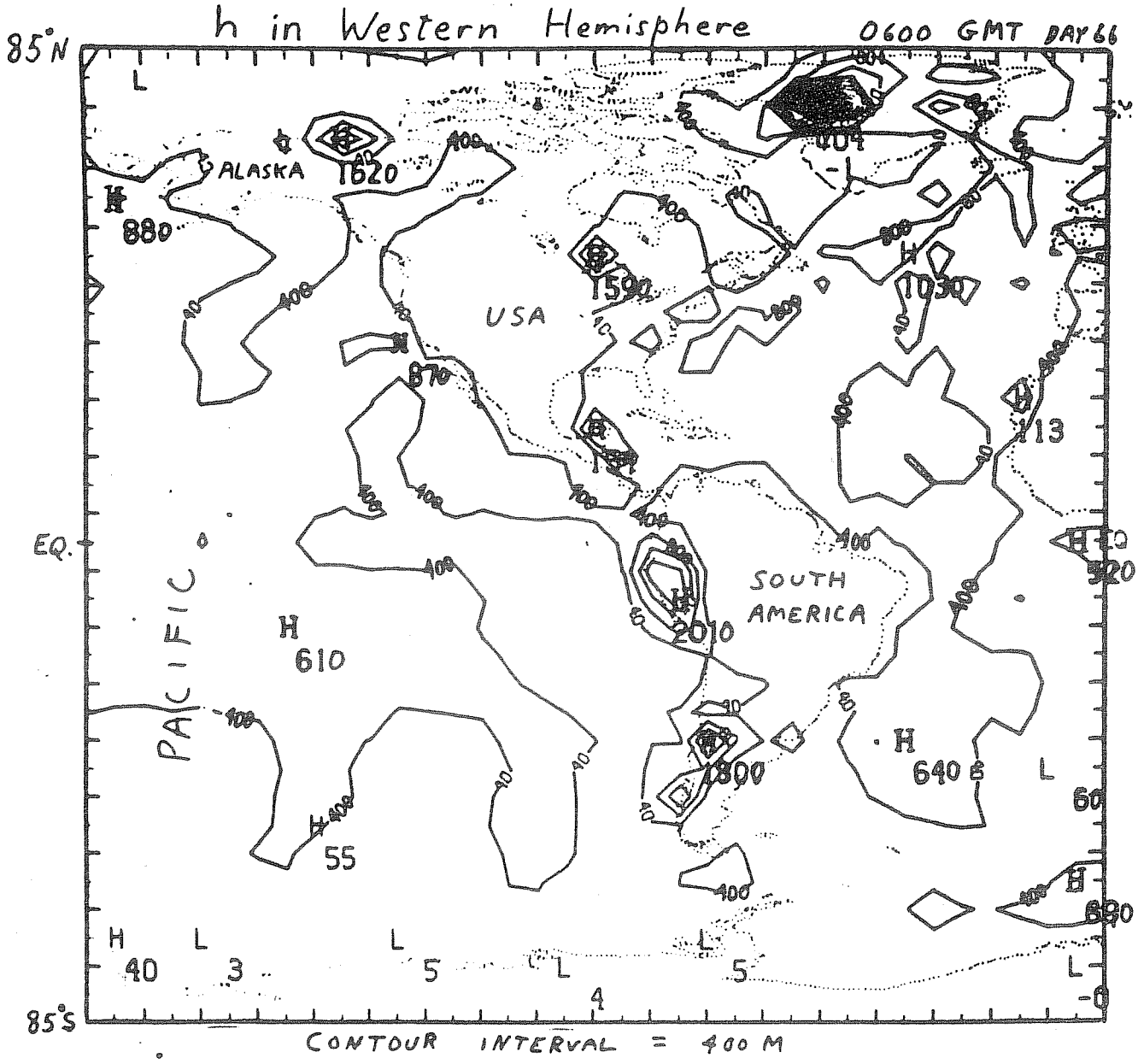

Fig. 6.5. The field of h(x,y) calculated for 0600 Greenwich Meridian Time (GMT) on DAY 66 in the western hemisphere.

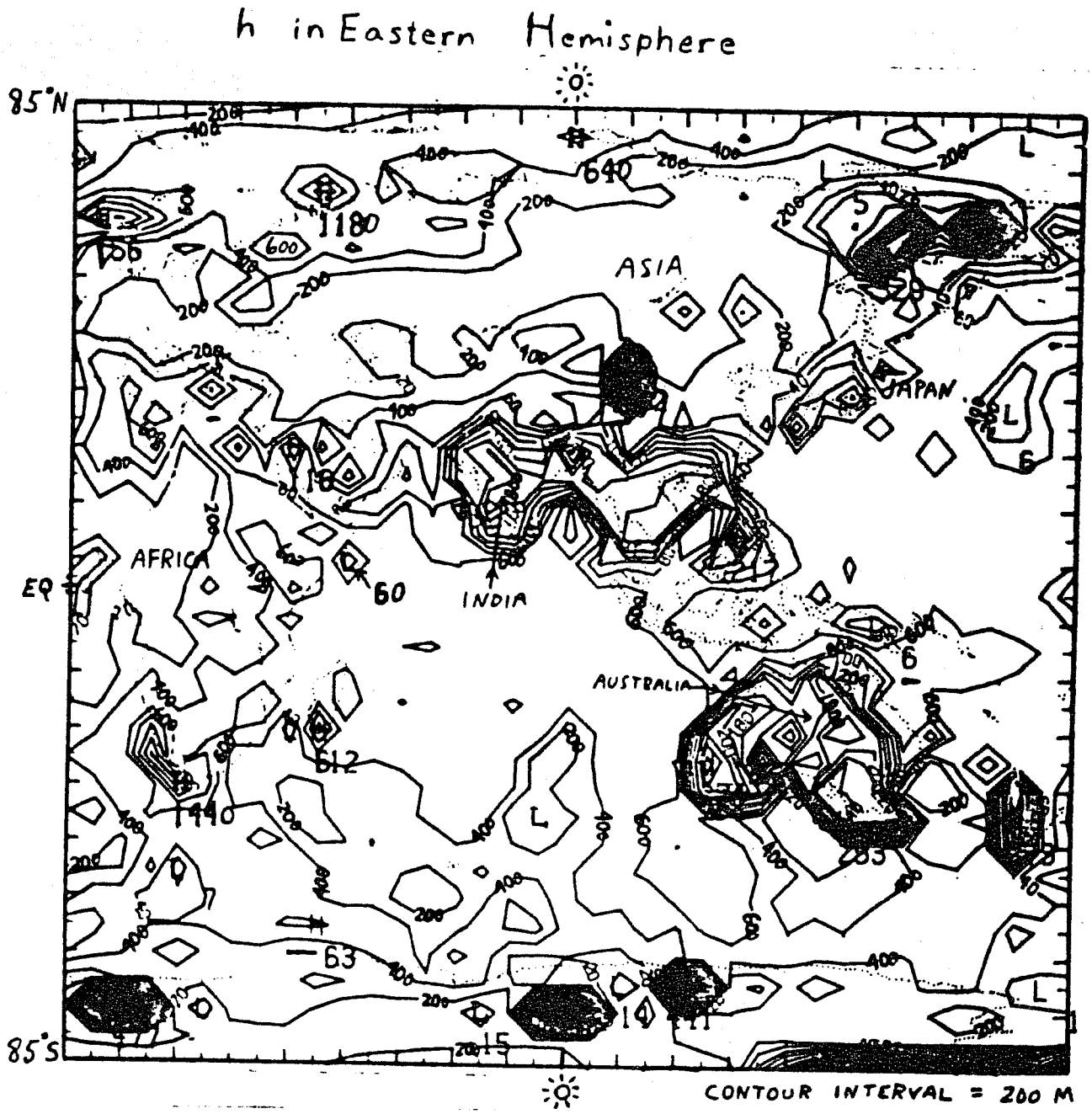

Fig. 6.6. The field of h(x,y) calculated for 0600 GMT on DAY 66 in the eater hemisphere.

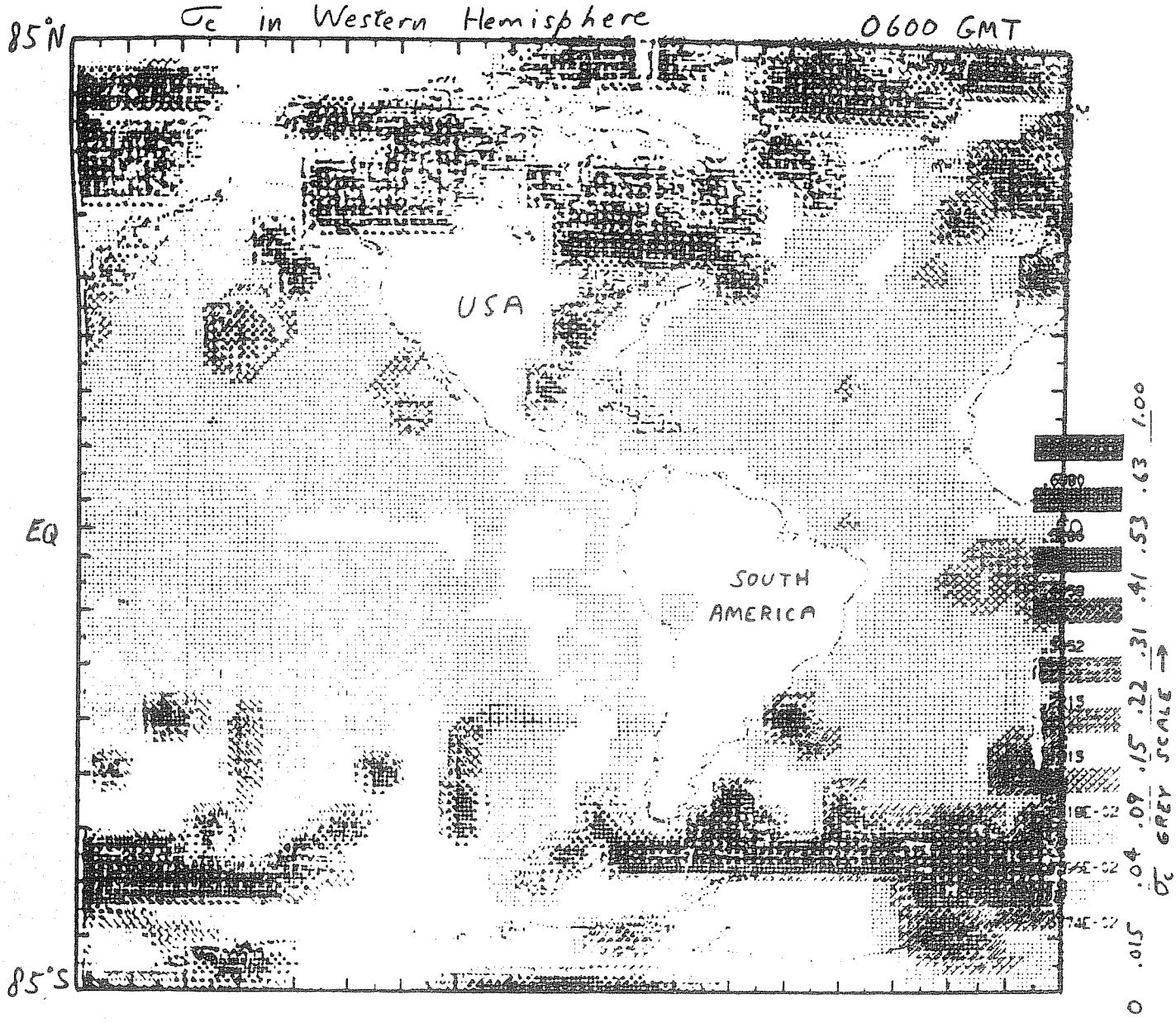

Fig. 6.7. The field of boundary-layer cloud fraction, σ_c, calculated for 0600 GMT on DAY 66 in the western hemisphere.

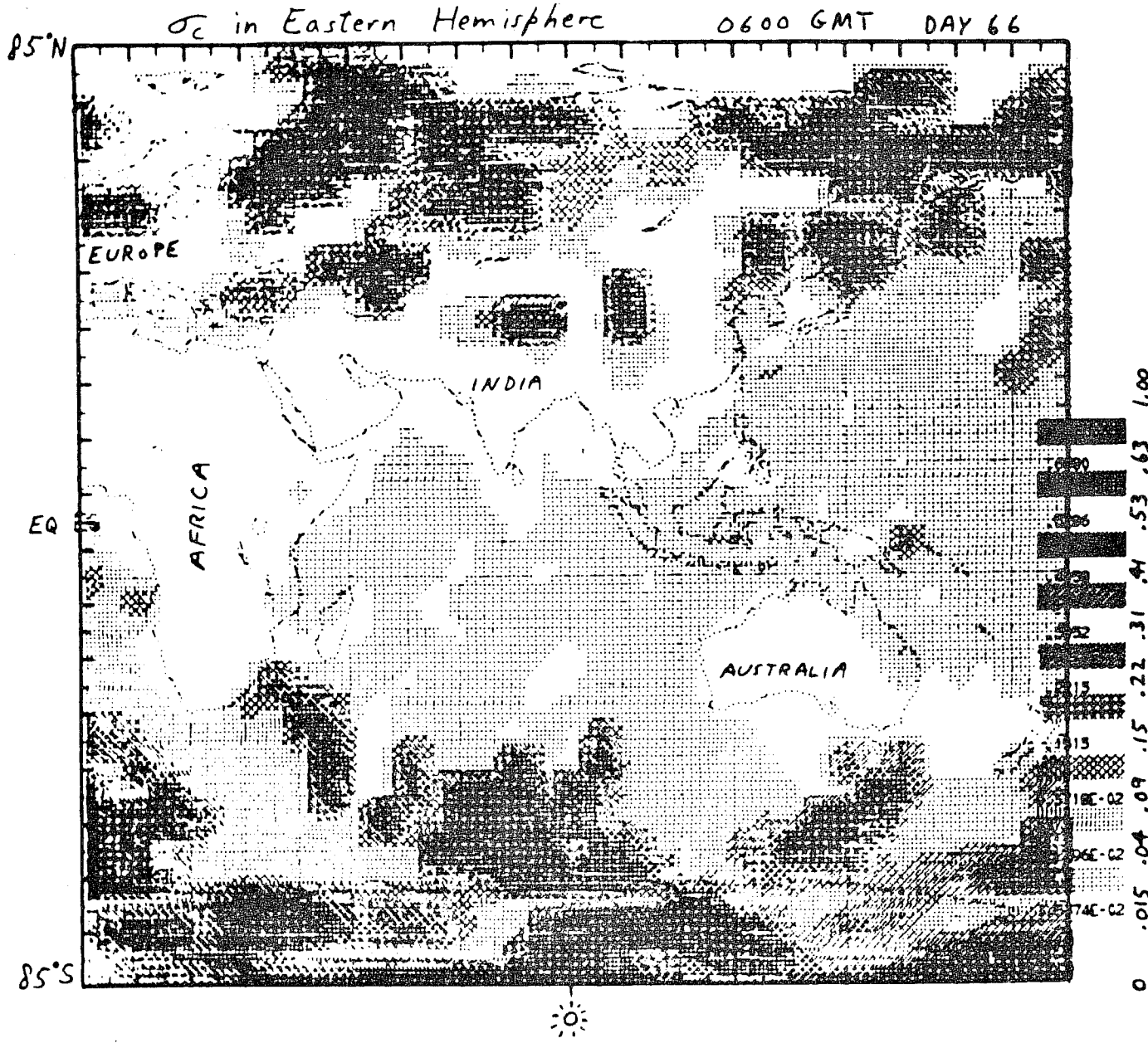

Fig. 6.8. The field of boundary-layer cloud fraction, σ_c, calculated for 0600 GMT on DAY 66 in the eastern hemisphere.

by Schubert (1976) to be favored positions for stratocumulus in July but not in January.

The global (grid-point weighted) average BL cloud cover predicted for this time was 0.14; 31% of the grid points were predicted to have no BL clouds because of stable stratification in the surface layer, 13% with unstable stratification were also clear, 47% had scattered cumulus, and 9% had stratocumulus.

6.4 Preliminary assessment of differences obtained between the boundary-layer (BL) and standard versions

This preliminary assessment is from the thesis of Benoit (1976) and is very tentative, as this first ten-day test run has suggested numerous small revisions to the parameterization, some of which may alter subsequent results substantially.

6.4.1 Surface pressure fields, p_s. Difference maps of p_s after 12, 24 and 36 hours of integration disclosed peak differences of about 4, 5 and 9 mb, respectively, in midlatitudes. These differences reflected mainly the differences in positions of traveling Lows. After about five days, however, even the central pressures of the best defined traveling Lows deviated by up to 10 or 15 mb. A lowering of the zonal mean p_s in the 50-60° S latitude belt by about 3 mb occurred in the first one and one-half days, with deeper and more numerous cyclones there. Surface winds in the BL version are now observed to flow across the isobars towards lower pressure at reasonable angles, whereas in the standard version they have the direction of the wind at 1.5 km where the flow may not even reflect the presence of a low pressure area at the surface.

6.4.2 Tropospheric temperatures. A marked decline in zonally averaged temperature, of from 3-5 C, occurred in equatorial regions in the first six days of the BL integration; after this little further change occurred. Mean cooling of 1-2 C occurred at 50° N and S. This change is believed due to a reduction in convective precipitation also noticed.

6.4.3 Specific humidity in the troposphere. Increased values of q at the 1.5 km level occurred over Africa, Australia, southern South America and eastern North America of from 1 to 4×10^{-3} after ten days. Over the oceans q was typically reduced at z = 1.5 km by 2×10^{-3}.

6.4.4 Precipitation. The same cloud-precipitation parameterization used in both versions of the GCM yields a few isolated grid points at which a large amount of convective precipitation occurs at any one time. The average intensity of these isolated centers of precipitation decrease from 24 cm day^{-1} to 16 cm day^{-1} in the BL version. The associated decrease in latent heating of condensation presumably led to the reduced temperatures already mentioned. A readjustment in the locations of net precipitation and evaporation also occurred, with a decrease of up to 3.7 cm of water from the soil just to the lee of the Rocky Mountains and an increase of up to 3.4 cm to the soil of the state of Tennessee during the ten-day period. The soil wetness in south-central Africa also increased substantially, and also in Indonesia; the Pampas of Argentina became drier. These and most of the other observed changes of soil wetness appear to be in the proper direction.

6.4.5 The wind field. The surface-layer trade wind circulation is much more correctly specified in the BL version, with the zonal average of the N-S component at 15° N being about -1.2 m s^{-1} in contrast with only -0.2 m s^{-1} in the standard version. However, the strength of the Hadley cell (from 1.5 km up) was not increased, but decreased slightly due to the increased surface stress. Higher up, zonal mean wind components appeared very similar in pattern and magnitude in both versions except in polar regions where a few points of excessive wind speed (already discussed) in the boundary layer version appeared in the lower troposphere. An unexplained quirk of the standard version is the existence of only a very narrow belt of weak westerlies at the surface in the Southern Hemisphere, between 42° S and 50° S. With the BL version this discrepancy became worse, and the zonally averaged westerlies, on DAY 66, did not even quite reach the surface in the Southern Hemisphere. It would take a much longer period of integration to determine how persistent this feature was.

6.4.6 Large-scale vertical velocities, $\bar{w}$. The patterns of $\bar{w}$ at 3 km appeared very similar in both versions. However, the rms values over the tropical Pacific on DAYS 63 and 66 had decreased from .85 (standard version) to .70 cm s^{-1} (BL version), while they had increased by similar amounts over the Pacific between 25° N and 60° N, and also over North America. It would thus not be entirely consistent to ascribe the change in rms $\bar{w}$ values to the strongly reduced drag coefficient over the oceans in the BL version. Instead, Benoit (1976) ascribes it to an increased horizontal smoothness in the surface-layer wind and stress fields observed over the tropical oceans in the BL version, leading to somewhat reduced magnitude of convergence and divergence there, and in $\bar{w}$ at 3 km. The increased smoothness in the tropics seems to result from prognosing (and horizontally advecting) the surface-layer wind rather than diagnosing it, in a region of relatively flat pressure field. In more temperate latitudes, where the surface pressure field is much more variable, the prognosed surface-layer winds and stresses are therefore more variable because they are driven by the pressure gradients which are spatially more variable in direction at sea level than at 1.5 km.

The reduced rms $\bar{w}$ values in the tropics are conjectured to be the cause of the reduced precipitation from the subgrid cloud-precipitation parameterization, and of the cooling observed in the BL version. This convective parameterization comes from a development of Krishnamurti and Moxim (1971), and the intensity of the heating by condensation is roughly proportional to $\bar{w}$ at 3 km for the usual case of a cloud base being diagnosed to occur within the lowest 3 km layer of the GCM.

6.4.7 Ground temperature and sensible heat flux. With the inclusion of a realistic soil heat-flux term in the surface energy balance of the BL version, the ground temperature (T_g) is as much as 12 C cooler in the daytime and up to 12-15 C warmer at night. An exception occurs over snow covered surfaces where the BL version yields cooler surface values. An even more important reason for the decreased T_g values in daytime over soil is the increased bulk aerodynamic heat transfer coefficient in the BL version, associated with increased z_0 over land (20 cm instead of 1.7 cm) and the use of Monin-Obukhov similarity. A greater fraction of the heat delivered to the atmosphere occurs via the sensible heat flux term rather than the $-T_g^4$ term, in the BL version. Hence, T_g is strongly reduced in the daytime, thereby yielding nearly the same values of sensible heat flux as from the standard version.

Not only were the zonal means of $(\overline{wT})_0$ the same within about 5% in the two versions at most latitudes (on DAY 66) but even the longitudinally dependent values along 15° N differed by about only ±30% on the average. This seems to indicate that the standard-version procedure of not allowing the surface-layer wind to drop below 5 m s^{-1} was working remarkably well, since this condition had been enforced at most of the grid points of the standard version. An exception was excessively negative values of sensible heat flux in polar regions from the standard version which incorporates too weakly the influence of stable stratification in suppressing the turbulent fluxes. In the BL version, the cooler surface temperatures over the snow surfaces led to a strong reduction in the magnitude of the sensible heat flux.

6.4.8 Evaporation rate. On DAY 66 zonally averaged values of the evaporation rate were virtually identical, except for 10% larger values in the BL version in the 10° N - 15° N belt and the 25° N - 40° N belt. This much agreement was quite surprising in view of the fact that the standard version rather arbitrarily reduces its bulk-aerodynamic moisture transfer coefficient by 30% relative to the heat-transfer coefficient. The BL version assumes the two to be identical.

In summary, this first ten-day run has demonstrated that a BL parameterization which takes explicit cognizance of the depth of the boundary layer and fraction of BL cloudiness, and one in which BL free-convection arguments play a large role, can be made to work successfully. Already the virtues of the new approach appear to outweigh disadvantages associated with several details still requiring improvement and debugging. In addition, it appears that the subgrid-scale precipitation parameterization will need to be improved and made compatible with the BL parameterization.

7. Outstanding problems remaining in boundary-layer parameterization

Most of the problems have already been touched upon. The more important ones will be listed here, in roughly estimated order of importance, first those that would affect almost any parameterization of the boundary layer and, secondly, those additional problems which affect the particular approach described in section 6.

7.1 Problems common to almost all BL parameterizations

1. It is not yet known how to treat the boundary layer under highly "disturbed" conditions when no clear demarcation exists between cloud-layer and subcloud-layer turbulence, and/or when precipitation induced downdraughts link the two layers.

2. Even under "undisturbed" conditions, a BL parameterization needs to be coupled with a cloud convection parameterization. Questions arise such as "Should we take account of the fact that some convective clouds have bases which are located above the BL?"

3. z_0 should be made a function of small-scale topography, dependent upon location.

4. Revised Monin-Obukhov empirical relations are needed for large-scale horizontal averages over rather heterogeneous terrain, and not just for Kansas-type terrain. This is especially true for the formulations of the stable surface layer.

5. Parameterization is needed of the main effects of ground cover (vegetation) upon the lower boundary conditions. These include the effects of radiative shielding upon ground temperature, and foliage temperature and transpiration upon sensible and latent heat fluxes.

6. A reliable parameterization is needed for the differences between the effective "roughness lengths" for temperature and moisture, and that for momemtum for various types of land surfaces.

7.2 Problems facing the comprehensive BL parameterization designed for a GCM with coarse vertical resolution

1. The present method of estimating the jumps in properties at the top of the BL is very crude. This is done by utilization of 10 m values and GCM values from 1.5, 4.5...km. If the consequences are later judged inacceptable due to resulting errors, there would appear to be no recourse but to switch to an entirely different parameterization built upon the use of a large number (8 to 12) GCM levels in the lowest 3 km above the surface.

2. There is occasional incompatibility between the predicted 10 m value of a variable and the 1.5 km GCM value of the same variable when the BL is of order 3 km in height. Fortunately, the entrainment fluxes act in the sense of minimizing such discrepancies.

3. Some effects of the variability of both h and the LCL within a large GCM grid area should be taken into account in the parameterization of the vertical fluxes due to entrainment at $z = h$. Presently, these fluxes are estimated by means of the theory which assumes the transition layer at $z = h$ to have infinitesimal thickness.

4. The estimates of BL cloud fraction and of cloud-induced subsidence utilized in the entrainment-rate equation need to be derived in conjunction with results of the cloud-convection-precipitation parameterization, and not estimated independently.

5. The influence of stable stratification in promoting vertical gradients within the boundary layer is presently ignored and needs to be taken into account. The present BL parameterization utilizes properties at 10 m, and the value of h, to assess the possible presence of stratocumulus as if the BL were well mixed. The BL might be declared unstable only because of the occurrence of cloud-top radiative cooling, the existence of which might not be predicted if properties near $z = h$ had been estimated on the basis of a stable BL rather than an unstable one.

6. The shape of the vertical-flux profiles within the stable boundary layer needs to be better determined from observations. The present parameterization assumes linear heat and moisture fluxes, mostly on the basis of theoretical studies.

7. The present parameterization does not permit the BL height to drop fast enough over land after sunset.

8. The parameterization of the influence of especially strong baroclinicity associated with mountain slopes upon surface-layer winds needs improvement.

9. The parameterization of the means by which stratocumulus breaks into scattered cumulus needs improvement.

10. Some account of BL fluxes of entrainment should be taken into account in the stable boundary layer, rather than assuming that they are then zero.

11. Revised boundary-layer growth equations for the stable BL should include influences of variable topography in enhancing the growth rate.

12. The influence of radiative cooling in altering the shape of the turbulent heat-flux profile, especially within the stable BL, needs more investigation and eventual inclusion within the prediction equations for the 10 m temperature. Also needing parameterization is the shortwave radiative warming as it affects the temperature at a height of 10 m.

13. The predicted entrainment rate atop a stratocumulus deck presently turns out too large when $\Delta\theta_e$ becomes very small or somewhat negative, since the entrainment formula is then close to its singular point of inapplicability. The "free" entrainment rate then utilized in its place appears to be too large on upper limit, and a more reasonable upper limit needs to be developed, perhaps some form of an encroachment equation, when stable stratification exists above the cloud deck. Furthermore, the closure assumption for forced entrainment in the presence of stratocumulus appears to need even further improvement.

14. An optimal interpolation formula for the entrainment rate between limits of free and forced convection, including the effects of the Coriolis parameter, and allowing for encroachment and/or free entrainment, needs development and testing against observations. In the present formula being utilized for entrainment, the interpolation was devised merely on the basis of simplicity.

15. The parameterization of soil moisture should be treated in almost as much detail as that given to ground temperature in order that the evaporation rate be as well estimated as the sensible heat flux. In the present BL parameterization, for example, and in most other parameterizations too, the surface does not even become wet until after many centimeters (usually) of rain have fallen.

16. Effects of a small, negative lapse rate of mean specific humidity within the mixed layer need to be included. This would result in somewhat higher cloud bases and mixed-layer depths when cumulus is present, and slightly smaller values of $-\Delta q$.

17. The ground-snow subsurface treatment of the parameterization needs abbreviation and simplification, if possible, so that it will not occupy a disproportionate fraction of the increased computer time and storage of the new BL parameterization. The new BL parameterization presently requires 70% more computer time than the standard version, and about half of this increase is involved with the subsurface soil treatment.

18. A consistent method of calculating the horizontal-advection terms in the surface-layer prognostic equations is needed to replace the present use of an upstream-Lagrangian approach at about one-third of the grid points and a second-order method at the other two-thirds of the grid points. The former method numerically damps, while the latter method can lead to fictitiously values at grid points having the same value of a property on the upstream side and a greatly different value (as caused by topographical differences, for example) on the downstream side.

19. Presently there is uncertainty in the depth below a stratocumulus cloud top to which the effective radiative cooling extends. We need observations and theory which agree on this.

20. Horizontal advection of h is not presently included within our growth rate equation for h.

21. When fog is present at the 10 m level in the stable surface layer, radiative cooling at its top may transform the layer into a weakly unstable layer. However, without vertical resolution between 10 m and 1.5 km, it is difficult to assess the fog's thickness and its radiative properties.

Apparently, a truism which cannot be avoided is that the more comprehensive and physically realistic a parameterization is made, in an attempt to make use of existing BL knowledge, the greater is the need for even more knowledge on how the atmospheric boundary layer behaves.

LIST OF REFERENCES

Arakawa, A., 1966: Computational design for long-term numerical integration of the equations of fluid motion: Two-dimensional incompressible flow, Part I. J. Comp. Phys., 1, 119-143.

Augstein, E., H. Schmidt and F. Ostapoff, 1974: The vertical structure of the atmospheric planetary boundary layer in undisturbed trade winds over the Atlantic Ocean. Bound.-Layer Meteor., 6, 129-150.

Benoit, R., 1976: A comprehensive parameterization of the atmospheric boundary layer for general circulation models. Ph.D. thesis, Department of Meteorology, McGill University, Montreal, Canada, 269 pp.

Betts, A. K., 1973: Non-precipitating cumulus convection and its parameterization. Quart. J. Roy. Meteor. Soc., 99, 178-196.

Carson, D. J., 1973: The development of a dry inversion-capped convectively unstable boundary layer. Quart. J. Roy. Meteor. Soc., 99, 450-467.

Carson, D. J., and F. B. Smith, 1974: Thermodynamic model for the development of a convectively unstable boundary layer. Adv. in Geophys., 18A, Academic Press, London, 111-124.

Cattle, H., and K. Weston, 1975: Budget studies of heat flux profiles in the convective boundary layer over land. Quart. J. Roy. Meteor. Soc., 101, 353-363.

Clarke, R. H., A. J. Dyer, R. R. Brook, D. G. Reid, and A. J. Troup, 1971: The Wangara Experiment: Boundary Layer Data. Tech. Paper No. 19, CSIRO, Division of Meteor. Physics, Australia, 359 pp.

Deardorff, J. W., 1972: Numerical investigation of neutral and unstable boundary layers. J. Atmos. Sci., 29, 91-115.

Deardorff, J. W., 1974: Three-dimensional numerical study of the height and mean structure of a heated planetary boundary layer. Bound.-Layer Meteor., 7, 81-106.

Deardorff, J. W., 1976a: Usefulness of liquid-water potential temperature in a shallow-cloud model. J. Appl. Meteor., 15, 98-102.

Deardorff, J. W., 1976b: On the entrainment rate of a stratocumulus-topped mixed layer. To appear in Quart. J. Roy. Meteor. Soc.

Esbensen, S., 1975: An analysis of subcloud-layer heat and moisture budgets in the western Atlantic Trades. J. Atmos. Sci., 32, 1921-1933.

Krishnamurti, T. N., and W. J. Moxin, 1971: On parameterization of convective and non-convective latent heat release. J. Atmos. Sci., 10, 3-13.

Lenschow, D. H., 1973: Two examples of planetary boundary layer modification over the Great Lakes. J. Atmos. Sci., 30, 568-581.

Lilly, D. K., 1965: On the computational stability of numerical solutions of time-dependent non-linear geophysical fluid dynamics problems. Mon. Wea. Rev., 93, 11-26.

Lilly, D. K., 1968: Models of cloud-topped mixed layer under a strong inversion. Quart. J. Roy. Meteor. Soc., 94, 292-309.

Mahrt, L. , and D. H. Lenschow, 1976: Growth dynamics of the convectively mixed layer. J. Atmos. Sci., 33, 41-51.

McEwen, A. D., and G. W. Paltridge, 1976: Radiatively driven thermal convection bounded by an inversion--A laboratory simulation of stratus clouds. J. Geophys. Res., 81, 1095-1102.

Ogura, Y. and H.-R. Cho, 1974: On the interaction between the subcloud and cloud layers in tropical regions. J. Atmos. Sci., 31, 1850-1859.

Schubert, W. H., 1976: Experiments with Lilly's cloud-topped mixed layer model. J. Atmos. Sci., 33, 436-446.

Sommeria, G., 1976: Three-dimensional simulation of turbulent processes in an undisturbed Trade Wind boundary layer. J. Atmos. Sci., 33, 216-241.

Tennekes, H., 1973: A model for the dynamics of the inversion above a convective boundary layer. J. Atmos. Sci., 30, 558-567.

Washington, W. M., 1974: NCAR global circulation model. In GARP Publication Series 14, "Modelling for the first GARP global experiment," World Meteorol. Organization, Int. Council of Sci. Unions, pp. 61-78.

Willis, G. E., and J. W. Deardorff, 1974: A laboratory model of the unstable planetary boundary layer. J. Atmos. Sci., 31, 1297-1307.